# A phospho-regulated ensemble signal motif of $\alpha$-TAT1 drives dynamic microtubule acetylation

Abhijit Deb Roy, Evan Gross, Gayatri Pillai, Shailaja Seetharaman, Sandrine Etienne-Manneville, Takanari Inoue

# A phospho-regulated ensemble signal motif of α-TAT1 drives dynamic microtubule acetylation

Abhijit Deb Roy[1*], Evan G. Gross[2], Gayatri S. Pillai[2], Shailaja Seetharaman[3,4], Sandrine Etienne-Manneville[3], Takanari Inoue[1*]

[1] Department of Cell Biology and Center for Cell Dynamics, Johns Hopkins University School of Medicine, 855 North Wolfe Street, Baltimore, MD 21205, USA

[2] The Johns Hopkins University, Baltimore, MD 21218, USA

[3]Cell Polarity, Migration and Cancer Unit, Institut Pasteur, UMR3691 CNRS, Equipe Labellisée Ligue Contre le Cancer, F-75015, Paris, France.

[4]Université Paris Descartes, Sorbonne Paris Cité, 12 Rue de l'École de Médecine, 75006 Paris, France.

[*] Correspondence:
Abhijit Deb Roy abhijit.debroy@gmail.com
Takanari Inoue jctinoue@jhmi.edu

**Abstract:**

Spatiotemporal patterns of microtubule modifications such as acetylation underlie diverse cellular functions. While the molecular identity of the acetylating agent, α-tubulin N-acetyltransferase 1 (α-TAT1), as well as the functional consequences of microtubule acetylation have been revealed, the molecular mechanisms that regulate multi-tasking α-TAT1 action for dynamic acetylation remain obscure. Here we identified a signal motif in the intrinsically disordered C-terminus of α-TAT1, which comprises three functional elements - nuclear export, nuclear import and cytosolic retention. Their balance is tuned via phosphorylation by serine-threonine kinases to determine subcellular localization of α-TAT1. While the phosphorylated form binds to 14-3-3 adapters and accumulates in the cytosol for maximal substrate access, the non-phosphorylated form is sequestered inside the nucleus, thus keeping microtubule acetylation minimal. As cancer mutations have been reported to this motif, the unique ensemble regulation of α-TAT1 localization may hint at a role of microtubule acetylation in aberrant physiological conditions.

## Introduction:

Acetylation of Lysine-40 of α-tubulin is an evolutionarily conserved post-translational modification observed across eukaryotic species[1–3], which is involved in diverse physiological and pathological states[4–6]. Acetylation is mainly observed in polymerized microtubules[7–9] and may provide structural flexibility to stabilize microtubules against bending forces[10–13]. In cultured cells, microtubule acetylation mediates focal adhesion dynamics, adaptation to extracellular matrix rigidity as well as regulation of tissue stiffness[14–17]. Additionally, acetylated microtubules regulate touch sensation in *M. musculus*, *C. elegans* and *D. melanogaster,* suggesting a role in mechano-response[18–21]. Microtubule acetylation has been implicated in axonal transport in neurons[22–24], migration in cancer cells[5,25–27], autophagy[6,28,29], podosome stabilization in osteoclasts[30] and viral infections[31–34]. α-TAT1 is the only known acetyltransferase for α-tubulin[35,36] in mammals. α-TAT1 predominantly catalyzes α-tubulin in stable polymerized microtubules[19,37], and may have additional effects on microtubules independent of its catalytic activity[38].

Although microtubule acetylation is spatially and temporally regulated downstream of many molecular signaling pathways, little is known about how these pathways converge on α-TAT1 to achieve such dynamic patterns. In the present study, we used computational sequence analyses and live cell microscopy to identify a conserved motif in the intrinsically disordered C-terminus of α-TAT1, consisting of an NES and an NLS, that mediates its spatial distribution. We show that cytosolic localization of α-TAT1 is critical for microtubule acetylation. We further demonstrate that nuclear localization of α-TAT1 is inhibited by the action of serine-threonine kinases, specifically cyclin dependent kinases (CDKs), Protein Kinase A (PKA) and Casein kinase 2 (CK2) and identify 14-3-3 proteins as binding partners of α-TAT1. Our findings establish a novel role of the intrinsically disordered C-terminus in

controlling α-TAT1 function by regulating its intracellular localization downstream of kinase and phosphatase activities.

## Results:

**α-TAT1 localization mediates microtubule acetylation:** α-TAT1 has an N-terminal catalytic domain that shows homology to other acetyltransferases, while its C-terminus was not resolved in crystal structures[39] (Fig. 1a). Based on its amino acid sequence, α-TAT1 C-terminus was predicted to be intrinsically disordered by both IUPred2A[40] and PrDOS[41] prediction servers (Fig. 1a, Supplementary Fig. S1a, b, c). To explore if the intra-cellular localization of α-TAT1 is regulated, we sought to identify any localization signals present in the α-TAT1 amino acid sequence (Supplementary Fig. S1a). The prediction program NetNES[42] identified a putative NES in α-TAT1 C-terminus (Fig. 1a, Supplementary Fig. S2). On the other hand, PSORT-II[43] subcellular localization program predicted that α-TAT1 should be predominantly localized to the nucleus due to the presence of a putative class 4 NLS[44] in its C-terminus (Fig. 1a). The region encompassing the putative NES and NLS is conserved across the human α-TAT1 isoforms (Supplementary Fig. S3a), as well as across mammalian α-TAT1 proteins (Supplementary Fig. S3b). To test whether α-TAT1 indeed showed any intracellular distribution pattern, we expressed mVenus-α-TAT1 in HeLa cells, and observed distinct nuclear exclusion in most cells, although a subset of cells showed lack of exclusion (Fig. 1b). Based on our categorization of the distribution patterns (see Methods, Fig. 1c), we determined that approximately 77% of cells showed cytosolic distribution, 22% showed diffused pattern (i.e., both cytosolic and nuclear distribution) and 1% of cells showed nuclear enrichment of mVenus-α-TAT1 (Fig. 1d). These observations were consistent with ratiometric analysis (see Methods, Fig 1c) of mVenus-α-TAT1 distribution (Fig. 1e). Time lapse microscopy showed temporal changes in fluorescence intensity of mVenus-α-TAT1 in cell nuclei and cytosol (Supplementary Fig. S4a, b), suggesting that α-TAT1 localization is dynamic by nature.

α-TAT1 preferentially acetylates polymerized microtubules, which are typically cytosolic. Based on this, we hypothesized that spatial regulation of α-TAT1 may control its function. Exogenous expression of mVenus-α-TAT1 or its catalytic domain (residues 1-236)[19,39] (Fig. 1f) was sufficient to significantly increase α-tubulin acetylation in HeLa cells compared to non-transfected cells (Fig. 1g, h). To test whether nuclear localization may sufficiently sequester α-TAT1 from microtubules, we tethered the NLS from cMyc to α-TAT1 catalytic domain and thus localized it to the nucleus (Fig. 1f, g top panel). Exogenous expression of NLS-mVenus-α-TAT1(1-236) did not increase α-tubulin acetylation levels compared to non-transfected cells (Fig. 1 g, h), suggesting that nuclear sequestration of α-TAT1 inhibits its function.

**α-TAT1 undergoes Exportin 1 dependent nuclear export:** To dissect the molecular mechanisms of α-TAT1 localization in the cytosol, we speculated that α-TAT1 is actively exported out of the nucleus, and/or that α-TAT1 binds to a protein that keeps the complex out of the nucleus. We began by testing the first possibility by assessing involvement of the nuclear export machinery. Exportin 1 (Exp1), also called Chromosome region maintenance 1 protein homolog (CRM1), mediates nuclear export of many proteins[45,46]. GFP-α-TAT1, but not GFP, co-immunoprecipitated with endogenous Exp1 (Fig. 2a), indicating an interaction between these two proteins. Treatment with 100 nM Leptomycin-B (LMB), an inhibitor of Exp1 mediated nuclear export[47], significantly decreased the number of cells displaying nuclear exclusion of mVenus-α-TAT1 compared to vehicle (Fig 2b, c, d). Inhibition of nuclear export was initiated within an hour of LMB treatment, although some cells were refractory to the treatment (Supplementary Fig. S5a, b). Decreased LMB concentrations (1 nM and 10 nM) had a comparable impact as 100 nM dosage (Supplementary Fig. S5c, d). Furthermore, LMB treatment induced significant reduction in α-tubulin acetylation levels in HeLa cells within 4

hours, compared to vehicle (Fig. 2e, f). Our data suggest that α-TAT1 is actively exported from the nucleus to the cytosol in an Exp1 dependent manner and that this export facilitates α-TAT1 function. The residual exclusion of α-TAT1 could be due to Exp1-independent nuclear export pathways or association with other cytosolic proteins, which was tested later (see below).

**Nuclear export of α-TAT1 is mediated by a C-terminal NES:** Our data demonstrate that α-TAT1 function is linked to Exp1 mediated nuclear export. To examine whether nuclear export of α-TAT1 is regulated by its catalytic activity, we expressed a catalytic dead mutant, mVenus-α-TAT1(D157N)[39], in HeLa cells. mVenus-α-TAT1(D157N) did not display any loss of nuclear exclusion (Supplementary Fig. S6a, b, c). The catalytic domain, mVenus-α-TAT1(1-236), displayed a complete loss of nuclear exclusion; whereas the C-terminus, mVenus-α-TAT1(236-323), displayed a distribution pattern comparable to that of WT (Fig. 3a, b, c, d). In addition, inhibition of Exp1 by 100 nM LMB significantly reduced the nuclear exclusion of mVenus-α-TAT1 C-terminus (Fig. 3e). Exclusion of α-TAT1 C-terminus (size $\approx$ 38 kDa) further indicates that nuclear exclusion of mVenus-α-TAT1 (size $\approx$ 63 kDa) is not simply due to size exclusion of passive diffusion into nuclei, and demonstrates that nuclear exclusion of α-TAT1 is a transferable property mediated by its C-terminus.

Exp1 dependent nuclear export is typically mediated by binding with short stretches of hydrophobic, often Leucine rich, NES[42,45] that are often found in disordered regions of the cargo proteins. As previously mentioned, NetNES suggested the presence of a conserved NES between V286 and L297 in α-TAT1 C-terminus (Supplementary Fig S2). Interestingly, this region is also predicted to be a site of protein-protein interactions by ANCHOR2 prediction software[40] (Supplementary Fig. S1b). Truncation of this putative NES, α-TAT1-delNES, abrogated its nuclear exclusion (Fig. 3a, b, c, d). Although alanine substitution of the

hydrophobic residues in the V286-L297 region, α-TAT1(VL/A), decreased its nuclear exclusion, the loss of exclusion was less than expected from our observations with LMB treatment (Supplementary Fig. S6a, b, c). On further examination of the NetNES prediction, we observed that the NES predicted by the Hidden Markov Model (Supplementary Fig. S2) included the residues between L282 and L297. Additional Alanine substitutions of L282 and F285, α-TAT1(NES/A) (Supplementary Fig. S6d), further reduced nuclear exclusion of α-TAT1 (Fig. 3a, b, c, d, Supplementary Fig. S6a, b, c), suggesting that these residues contribute to the nuclear export of α-TAT1. Taken together, our data suggest that α-TAT1 has a hydrophobic NES in its C-terminus.

**α-TAT1 interacts with 14-3-3 proteins.** Our observations thus far with nuclear exclusion of mVenus-α-TAT1 indicate that the putative NLS identified by the PSORT prediction server is either non-functional or is basally inhibited with occasional activation. 14-3-3 protein binding has been reported to negatively regulate nuclear import by inhibiting binding of importins to NLS[48–50]. Part of the putative NLS sequence “PAQRRRTR” bears similarity to 14-3-3 binding motif RXX(pS/pT)XP[51], and 14-3-3-Pred[52], a 14-3-3 interaction prediction server identified T322 as a potential 14-3-3 binding site. To examine whether α-TAT1 bound to 14-3-3 proteins, we co-expressed GFP-α-TAT1 with HA-tagged 14-3-3-β or 14-3-3-ζ in HEK-293T cells and performed a co-immunoprecipitation assay. GFP-α-TAT1, but not GFP alone, co-precipitated with HA-14-3-3-β and HA-14-3-3-ζ (Fig. 4a). These observations are consistent with our observations in mass spectrometry analysis of α-TAT1 in HEK cells that identified 14-3-3-β and 14-3-3-ζ as potential interactors[53].

**Serine/threonine kinase activities mediate cytosolic localization of α-TAT1.** 14-3-3 binding to proteins is mediated by phosphorylated serine and threonine residues[51]. NetPhos

prediction server identified over 30 putative phosphosites in α-TAT1, of which nine residues have been reported to be phosphorylated in phospho-proteomic studies (Supplementary Fig. S7a, b). Treatment with 100 nM Staurosporin, a pan-kinase inhibitor, significantly increased nuclear localization of α-TAT1 (Fig. 4b, c, Supplementary Fig. S8), suggesting that phosphorylation negatively regulated nuclear localization of α-TAT1. To identify the specific kinases that regulate α-TAT1 localization, we treated cells expressing mVenus-α-TAT1 with several serine-threonine kinase inhibitors (summarized in Supplementary Table T1). Both RO-3306 (inhibitor for CDK1 and CDK2[54,55]) and PD0332991 (also called Pablociclib, inhibitor for CDK4 and CDK6[56,57]), but not Purvalanol-B (inhibits CDK1, CDK2 and CDK5[55]), increased nuclear localization of mVenus-α-TAT1 in HeLa cells (Fig. 4b, c, Supplementary Fig. S8). Silmitasertib (also called CX-4945, inhibitor for CK2[58]) but not D-4476 (inhibitor for CK1[59]) also had a similar impact (Fig. 4b, c, Supplementary Fig. S8). Although H-89 (inhibitor for PKA) only had a moderate effect on mVenus-α-TAT1 localization, co-expression of mCFP-PKI, a more potent inhibitor for PKA[60], considerably increased nuclear localization of mVenus-α-TAT1 (Fig 4c, Supplementary Fig. S8, Supplementary Table T1). Finally, treatment with LJI308 (inhibitor for Ribosomal S9 kinase) appeared to further increase nuclear exclusion of mVenus-α-TAT1 (Fig. 4c, Supplementary Table T1). These data demonstrate that nuclear localization of α-TAT1 is negatively regulated by CDKs, CK2 and PKA.

**Nuclear localization of α-TAT1 is phospho-inhibited:** Since α-TAT1(1-284) did not display nuclear exclusion (Fig. 3b, c, d), we reasoned that the phosphosites which inhibit nuclear localization of α-TAT1 might be located between F285 and R323. NetPhos prediction server identified S294, T303, S315 and T322 as potential phosphosites in this region (Supplementary Fig. S7a, indicated in red box), wherein only S315 and T322 have been reported to be phosphorylated in phosphoproteomic studies (Supplementary Fig. S7b) and

they also flank the putative NLS (Fig. 5a). Importin-α binds with NLS enriched in basic residues through a charge-based interaction[44]. Phosphorylation of amino acids adjacent to such an NLS may inhibit the association of Importin-α binding through a disruption of the charge balance in the NLS region[61]. Alanine substitution of T322, but not of S315, significantly increased nuclear localization of mVenus-α-TAT1 (Fig. 5a, b, c, d, Supplementary Fig. S9a, b, c). Alanine substitution of both S315 and T322, α-TAT1(ST/A), showed considerably more nuclear localization of mVenus-α-TAT1 than T322 alone (Fig 5a, b, c, d). These data suggest that T322 phosphorylation inhibits nuclear localization of α-TAT1, while S315 may play a co-operative role in such inhibition. Substitution of S315 with acidic residues (S315D) appeared to boost nuclear exclusion of α-TAT1, whereas substitution of T322 with acidic residues (T322E) or both (ST/DE) displayed increased diffused pattern, but not increased nuclear accumulation (Supplementary Fig. S9a, b, c). This may be because these acidic residues, unlike phosphate moieties, do not sufficiently counter the basic residues in the NLS; or that phospho-T322, and to a lesser extent, phospho-S315 phosphorylation may be involved in protein-protein interactions, possibly with 14-3-3 isoforms, that inhibit nuclear localization of α-TAT1. These observations suggest that the phosphate moiety in phosphorylated T322 and S315 is critical for inhibition of α-TAT1 nuclear import.

One possible explanation of increased nuclear localization of T322A mutant is that phospho-T322 mediates nuclear export of α-TAT1. Truncation of the putative NLS including T322, α-TAT1-delNLS, did not increase nuclear localization (Fig. 5a, b, c, d), indicating that T322 did not mediate nuclear export of α-TAT1. Furthermore, alanine substitution of the hydrophobic residues in α-TAT1 NES as well as S315 and T322, α-TAT1(NES/A, ST/A) not only abrogated nuclear exclusion, but considerably increased nuclear accumulation of α-TAT1 (Fig. 5a, b, c, d), suggesting additive effects of NES inhibition and NLS activation. α-TAT1(NES/A, ST/DE) mutant also showed diffused pattern but not nuclear accumulation

(Supplementary Fig. S9a, b, c). Taken together, our observations suggest that phospho-T322 inhibits α-TAT1 NLS and that the α-TAT1 NES and NLS act independently of one another.

## Discussion:

One of the bottlenecks in elucidating the role of microtubule acetylation in biological phenomena is the knowledge gap of how upstream molecular signaling pathways control α-TAT1 function to modulate microtubule acetylation. Our study demonstrates that intracellular α-TAT1 localization is a dynamically regulated process, orchestrated by a balance of nuclear export and import, which modulates microtubule acetylation levels (Fig. 5e). To our knowledge, this is the first study to identify the molecular mechanisms that spatially regulate α-TAT1. We have demonstrated a hitherto unknown role of the inherently disordered α-TAT1 C-terminus and identified novel interactions with 14-3-3 proteins and several kinases. TAK1 dependent phosphorylation of α-TAT1 Serine-237 has been reported to stimulate its catalytic property[62]. In neurons, $p27^{kip1}$ directly binds to α-TAT1 and stabilizes it against proteasomal degradation[24], thus enhancing α-tubulin acetylation. Our observation that spatial sequestration of α-TAT1 from microtubules modulates acetylation dynamics suggests a role of the nucleus as a reservoir or sequestration chamber to control protein access of substrates. Regulated spatial sequestration of biomolecules can control their action[63–67] and aberrant localization of proteins have been reported in many diseases[68–71]. Our study further highlights the role of spatial signaling processes in controlling protein function.

We have demonstrated active nuclear export of α-TAT1 by Exp1 through an NES rich in hydrophobic residues, which was critical for efficient microtubule acetylation. In addition, we have identified an NLS consistent with non-canonical class IV NLS[44]. Interestingly, position 7 of this NLS, which should not be an acidic residue, is occupied by Threonine-322. Since phosphorylation of threonine can significantly increase its net negative charges, it is ideally situated to act as an ON/OFF switch for the NLS. Although we have identified Threonine-322 to be the critical phospho-residue that inhibits nuclear import, Serine-315 appears to provide

additional inhibition. The increased nuclear localization of ST/A mutant over T322A mutant raises the possibility that S315 and T322 may aggregate signals from different signaling pathways to fine-tune α-TAT1 localization.

Our data demonstrate that nuclear localization of α-TAT1 is inhibited by kinase action, possibly on Threonine-322 and Serine-315. Specifically, our study shows a role of CDKs, PKA and CK2 in coordinating spatial distribution of α-TAT1. Such phospho-regulation of α-TAT1 provides a possible mechanism for the changes in α-TAT1 localization and microtubule acetylation observed at different stages of the cell cycle[72]. We identified Threonine-322 to be a putative binding site for 14-3-3 proteins and demonstrated that α-TAT1 binds to 14-3-3-β and 14-3-3-ζ proteins. 14-3-3s typically interact with phospho-serines or phospho-threonines in intrinsically disordered regions and may mediate nuclear transport of proteins by masking NES or NLS[73]. Furthermore, 14-3-3 proteins may significantly alter the structure of their binding partners to align along their rigid α-helical backbone, to expose or hide critical binding sites[74]. Comparable kinase-mediated regulation of nuclear export and nuclear import has previously been reported in a few transcription regulators[75–78]. In particular, regulation of Cdc25 localization by Checkpoint kinase1 (Chk1) mediated phosphorylation of and subsequent recruitment of 14-3-3-β to an NLS-proximal phosphosite is virtually the same as our proposed model (Fig. 5e) of α-TAT1 localization[78,79], suggesting that such kinase-mediated balancing of nuclear export and import is a general strategy for protein localization. α-TAT1 is unique in this aspect in that unlike the other proteins that are spatially regulated in this manner, α-TAT1 has no known substrates in the nucleus and that its nuclear localization appears to be primarily to sequester it from microtubules. Of course, it is possible that nuclear import of α-TAT1 facilitates interactions with presently unidentified substrates located in the nucleus. In a similar vein, 14-3-3 proteins and Exp1 are also acetylated[80,81], and it is intriguing to speculate that these might be substrates of α-TAT1.

It is worthwhile to consider that a significant number of post-translational modifications of α-TAT1 appear on its intrinsically disordered C-terminus (Supplementary Fig. 7b). Disordered regions may act as a signaling hub by interacting with multiple proteins, thus facilitating complex formation and acting as integrators of signaling pathways[82]. We have demonstrated the presence of an NES, NLS, phosphorylation sites and putative 14-3-3 binding sites within the α-TAT1 C-terminus. That it is well conserved across mammalian species as well as in all the human isoforms suggests a critical role of the α-TAT1 C-terminus in its function. Indeed, numerous cancer-associated mutations curated in COSMIC[83] (www.cancer.sanger.ac.uk) and TCGA Research Network (www.cancer.gov/tcga) databases, in the ATAT1 gene are located in the intrinsically disordered C-terminal region. More specifically, there are a considerable number of deletions, frame shifts and missense mutations encompassing the NES and the NLS regions, which may be expected to affect the spatial distribution of α-TAT1. Whether these mutations underlie the pathogenesis in these cancers remain to be examined. Considering the role of microtubule acetylation in a wide array of cellular activities, it may be conjectured that loss of spatial regulation of α-TAT1 may be present in other diseases as well.

In conclusion, we propose a new model for regulation of microtubule acetylation through spatial sequestration of α-TAT1 (Fig. 5e), which include three key aspects: presence of an NES that facilitates Exp1 mediated nuclear export, presence of an NLS to mediate nuclear import and finally, modulation of this nuclear import by kinases. Further investigation into the role of specific kinases on α-TAT1 localization may yield a better understanding of its function in cellular processes and pathologies and help identify new therapeutic targets.

## Materials and Methods

**Cell culture and transfection:** HeLa and HEK-293T cells were cultured in DMEM basal media and passaged every third day of culture. For optimal growth, the media were supplemented with 10% (v/v) fetal bovine serum and Penicillin/Streptomycin, and the cells were maintained under standard cell culture conditions (37 °C and 5% $CO_2$). The cell lines were regularly checked for mycoplasma contamination. FuGENE 6 reagent (Promega, Madison, WI) was used for transient transfection of HeLa cells according to the manufacturer's instructions. For immunoprecipitation assays, HEK cells were transfected using calcium phosphate method.

**DNA plasmids:** H2B-mCherry construct was a generous gift from Dr. Sergi Regot. α-TAT1 construct was a generous gift from Dr. Antonina Roll-Mecak. The α-TAT1 construct was subcloned into the pTriEx-4 vector (Novagen) using PCR and restriction digestion with mVenus at the N terminus and α-TAT1 at the C terminus. H2B-mCherry and CFP-PKI constructs were respectively subcloned into mCherry-C1 and mCer3-C1 vectors (Clontech). GFP-αTAT1 construct was a gift from from Dr. Philippe Chavrier and Dr. Guillaume Montagnac. HA-14-3-3 plasmids were a generous gift from Dr. Michael Yaffe. As indicated in the results and figure legends, tags of compatible fluorescent proteins including Cerulean, mVenus and mCherry were appended to facilitate detection. Unless specified otherwise, the termini of tagging were positioned as in the orders they were written. Truncations of α-TAT1 were generated by PCR. Point mutations of α-TAT1 were generated using overlapping PCR. The open reading frames of all DNA plasmids were verified by Sanger sequencing.

**Sequence alignment:** Protein sequence alignment was performed using Clustal-W[84] (https://www.ebi.ac.uk/Tools/msa/clustalo/).

**Nuclear transport and kinase inhibitors:** LMB was purchased from LC Laboratories (catalog # L6100). SB203580 (Sigma Aldrich, catalog # S8307), Doramapimod (BIRB 796, Selleck Chemicals, catalog # S1574), CHIR99021 (Sigma Aldrich, catalog # SML1046), Sostrastaurin (Selleck Chemicals, catalog # S2791), RO-3306 (Selleck Chemicals, catalog # S7747), Ipatasertib (RG7440, Selleck Chemicals, catalog # S2808), Capivasertib (AZD5363, Selleck Chemicals, catalog # S8019), Silmitasertib (CX 4945, Selleck Chemicals, catalog # S2248), KU-55933 (Sigma Aldrich, catalog # SML1109) were generous gifts from Dr. Sergi Regot. SB239063 (Sigma Aldrich, catalog # S0569) was a generous gift from Dr. Jun Liu. The rest of the kinase inhibitors were purchased as indicated: Staurosporine (Sigma Aldrich, catalog # 569397), LJI308 (Sigma Aldrich, catalog # SML1788), Y-27632 (LC Laboratories, catalog # Y-5301), Gö 6976 (Sigma Aldrich, catalog # 365250), Gö 6983 (Sigma Aldrich, catalog # G1918), H-89 (Sigma Aldrich, catalog # B1427), D4476 (BioVision, catalog # 1770), KN-62 (Selleck Chemicals, catalog # S7422), KU-57788 (MedChemExpress, catalog # HY-11006), Purvalanol B (AdipoGen Life Sciences, catalog # SYN-1070), KT-5823 (Cayman Chemicals, catalog # 10010965), PD0332991 (Sigma Aldrich, catalog # PZ0199).

**Immunofluorescence assays:** HeLa cells were transiently transfected with mVenus-α-TAT1, mVenus-α-TAT1 catalytic domain and NLS-mVenus-α-TAT1 catalytic domain. 24 hours post-transfection, cells were fixed using ice-cold methanol for 10 minutes, washed thrice with cold PBS, blocked with 1% BSA in PBS for one hour and then incubated overnight at 4°C with monoclonal antibodies against tubulin (Millipore, catalog # MAB1864) and acetylated α-Tubulin (Sigma Aldrich, catalog # T7451). Next day, the samples were washed thrice with cold PBS and incubated with secondary antibodies (Invitrogen) for one hour at room temperature, after which they were washed thrice with PBS and images were captured by microscopy. For LMB treatment, HeLa cells were dosed with 100 nM LMB or equal volume of vehicle (EtOH),

incubated for 4 hours, after which methanol fixation and immunostaining was performed as described above.

**Immunoprecipitation assays:** HEK293T cells were transiently transfected with pEGFP-c1 (GFP-Ctl) or GFP-αTAT1 with HA-14-3-3β or HA-14-3-3ζ using the calcium phosphate method. Cell lysates were prepared by scraping cells using 1X lysis buffer (10X recipe- 50 mM Tris pH 7.5, triton 20%, NP40 10%, 2 M NaCl, mixed with cOmplete protease inhibitor tablet - Roche, Product number 11873580001). Cell lysates rotated on a wheel at 4°C for 15 min and centrifuged for 10 min at 13,000 rpm 4°C to pellet the cell debris. A small volume of the supernatant was used as the soluble input. Soluble detergent extracts were incubated with GFP nanobody (NanoTag, N0310) for 1 h at 4°C. Samples were then centrifuged and washed thrice with wash buffer (250 mM NaCl, 0.1% Triton X-100 in PBS). The resin and the soluble input were then mixed with Laemmli buffer (composed of 60 mM Tris-HCl pH 6.8, 10% glycerol, 2% SDS and 50 mM DTT with the addition of protease and phosphatase inhibitors). Samples were boiled 5 min at 95°C before loading in polyacrylamide gels. Gels were transferred for western blot and membranes were blocked with TBST (0.1% Tween) and 5% milk and incubated 1 h with the primary antibody and 1 h with HRP-conjugated secondary antibody. Bands were revealed with ECL chemiluminescent substrate (Biorad). Two different western blots were used to visualize GFP-Input and HA-14-3-3 proteins due to similar molecular weights. Antibodies used: GFP-HRP (NB600-313, Novus Biologicals), anti-HA (rat; Merck; 11867423001), anti-exportin-1 (mouse; BD Transduction Laboratories™; 611832). Secondary HRP antibodies were all purchased from Jackson ImmunoResearch.

**Microscopy and image analyses:** All imaging was performed with an Eclipse Ti microscope (Nikon) with a 100X objective (1.0X zoom and 4X4 binning) and Zyla 4.2 sCMOS camera (Andor), driven by NIS Elements software (Nikon). Time lapse imaging was performed at 15 min intervals for 10-15 hours. All live cell imaging was conducted at 37°C, 5% $CO_2$ and 90%

363 humidity with a stage top incubation system (Tokai Hit). Vitamin and phenol red-free media
364 (US Biological) supplemented with 2% fetal bovine serum were used in imaging to reduce
365 background and photobleaching. Inhibitors and vehicles were present in the imaging media
366 during imaging. All image processing and analyses were performed using Metamorph
367 (Molecular Devices, Sunnyvale, CA, USA) and FIJI software (NIH, Bethesda, MD, USA).

368 For categorical analysis of mVenus-α-TAT1 localization, images were visually
369 inspected and classified as displaying either cytosolic, diffused, or nuclear localization of
370 mVenus fluorescence signal. For ratiometric analysis, the ratio of the fluorescence intensity
371 from region of interest ($\approx$ 10 µm diameter) in the nucleus to that in a perinuclear area was
372 used to minimize any volumetric artifacts (Fig. 1c). To determine the baseline Nuc/cyto ratio
373 for cytosolic (<0.8) and nuclear (>1.2), we visually identified WT mVenus-α-TAT1 cells, with or
374 without LMB treatment, that showed distinctly cytosolic or nuclear localization and used the
375 rounded average ratio values from these cells (n > 100 cells). All cells showing nuc/cyto ratio
376 in between were classified as diffused. For both categorical and ratiometric analyses, H2B-
377 mCherry signal was used to identify nuclei; in a few cases where H2B-mCherry signal was
378 absent, phase images were used to identify the nuclei. Cells displaying too much (near
379 saturation in 16 bit) or too little (approximately less than 1.5-fold signal over background) of
380 mVenus or mCherry fluorescence signal, or those which appeared to be dying on visual
381 inspection were not included during image acquisition.

382 For immunofluorescence assays with exogenous expression of mVenus-α-TAT1
383 plasmids, transfected cells were identified by the presence of mVenus fluorescence signal.
384 The ratio of acetylated α-Tubulin over α-Tubulin (Ac. α-Tub/α-Tub) for transfected cells was
385 normalized against that for non-transfected cells averaged over 20 untransfected cells from
386 the same dish. For LMB and vehicle treatment, Ac. α-Tub/α-Tub ratios are shown.

**Statistical analyses:** Microsoft Excel (Microsoft, Redmond, WA, USA) and R (R Foundation for Statistical Computing, Vienna, Austria) were used for statistical analyses. Exact number of samples for each data set are specified in the respective figure legends. Data was pooled from at least three independent experiments (technical replicates) and within each experiment typically data from at least 40 cells were obtained (biological replicates). In some cases with kinase inhibitors that induced cell death, we collected data from smaller number of cells per experiment but increased the number of experiments to ensure sufficient data. Sample sizes were chosen based on the commonly used range in the field without performing any statistical power analysis. Normal probability plot (Supplementary Fig. S10) was utilized to confirm normal distribution of the Nuc/Cyto ratio of mVenus-αTAT1. Extreme outliers (<Q1 – 3xIQR or >Q3+3xIQR) were excluded from plots and statistical analyses. *P*-values were obtained from two-tailed Students *t*-test assuming unequal variance. Exact *P*-values for kinase inhibitor assays are available in Supplementary Table T1.

**Data availability:** All relevant data and source codes are included. Plasmid constructs will be available through Addgene.

## Acknowledgements

We thank Allen Kim for discussions that led to initiation of this project and Amy F. Peterson for help with the kinase inhibitor assays. We thank Yuta Nihongaki and Helen D. Wu for constructive discussions, as well as Robert DeRose for proofreading. This project was supported by American Heart Association fellowship 20POST35220046 (ADR), discretionary funds (TI), the La Ligue contre le cancer (S-CR17017) and Centre National de la Recherche Scientifique and Institut Pasteur. SS is funded by the ITN PolarNet Marie Curie grant and Fondation pour la Recherche Médicale and is enrolled at the Ecole Doctorale Frontières du Vivant (FdV) – Programme Bettencourt.

## Contributions

ADR initiated the project and designed and performed most of the experiments and data analyses. GSP and EGG performed experiments and data analyses under the guidance of ADR and TI. SS performed the immunoprecipitation assays under the guidance of SEM. ADR and TI wrote the final version of the manuscript based on contributions from all the authors.

## Competing interests

The authors declare no competing interests.

## Figure legends

**Figure 1. Intracellular distribution of α-TAT1 mediates its function.**

a) Cartoon showing predicted NES and NLS in intrinsically disordered C-terminus of α-TAT1, adapted from PDB: 4GS4, b) intracellular distribution of mVenus-α-TAT1, red dotted lines outline nuclei as identified by H2B-mCherry in lower panel, c) cartoon showing criteria for categorical and ratiometric analyses of α-TAT1 distribution, d) categorical analysis (n = 1032 cells) and e) ratiometric analysis (n = 304 cells) of mVenus-α-TAT1 localization, f) cartoon showing α-TAT1 mutants used in g) immunofluorescence assays showing levels of acetylated α-tubulin and total α-tubulin, transfected cells are indicated with red arrowheads, h) ratio of acetylated α-tubulin to total tubulin intensities with exogenous expression of α-TAT1 and its mutants, normalized against that of non-transfected cells, (WT: 50, catalytic domain: 44, NLS-catalytic domain: 48 cells). Scale bar = 10μm. ***: $P$<0.001 and NS: not significant, Student's *t*-test.

**Figure 2. α-TAT1 undergoes Exp1 mediated nuclear export.**

a) Co-immunoprecipitation of endogenous Exp1 with GFP-α-TAT1, b) intracellular distribution of mVenus-α-TAT1 with vehicle (EtOH) and 100 nM LMB treatment, nuclei are indicated in red dotted lines, c) categorical analysis (WT: 1032, vehicle: 450, LMB: 495 cells) and d) ratiometric analysis (WT: 304, vehicle: 210, LMB: 240 cells) of mVenus-α-TAT1 localization with vehicle and LMB treatment, e) immunofluorescence images showing acetylated and total α-tubulin in HeLa cells with vehicle or LMB treatment, f) ratio of acetylated to total α-tubulin with vehicle or LMB treatment (vehicle:120, LMB: 130 cells). Scale bar = 10μm. ***: $P$<0.001 and NS: not significant, Student's *t*-test.

**Figure 3. Intracellular distribution of α-TAT1 is mediated by its C-terminus.**

a) Cartoon showing α-TAT1 mutant design, b) categorical analysis (WT: 1032, Cat. Dom: 371, C-term: 290, delNES: 343 and NES/A: 501 cells) and c) ratiometric analysis (WT: 304, Cat. Dom: 213, C-term: 220, delNES: 221 and NES/A: 212 cells) of mVenus-α-TAT1 mutant localization as indicated, d) representative images showing intracellular distribution of mVenus-α-TAT1 mutants as listed, red dotted lines outline nuclei, e) ratiometric analysis of intracellular distribution of mVenus-α-TAT1 C-term with 100 nM LMB (C-term: 220, LMB: 209 cells. Scale bar = 10μm. ***: *P*<0.001 and NS: not significant, Student's *t*-test.

**Figure 4. Nuclear localization of α-TAT1 is phospho-inhibited.**

a) Co-immunoprecipitation of GFP-α-TAT1 with HA-14-3-3β and HA-14-3-3ζ proteins, b) intracellular distribution of mVenus-α-TAT1 with Staurosporine, RO-3306, PD0332991 and Silmitasertib treatment, nuclei are indicated in red dotted lines, c) ratiometric analysis of mVenus-α-TAT1 localization with kinase inhibitors (WT:304, STS: 183, RO-3306: 221, PD0332991: 234, Purvalanol-B: 243, D4476:253, Silmitasertib: 253, H89: 219, PKI: 208, Ipatasertib: 259, Capivsertib: 218, Go6976: 297, Go6983: 241, Sostrastaurin: 401, KT-5823: 269, SB203580: 259, Birb796: 262, KU55933: 317, LJI308: 229, CHIR99021: 227, KN-62:210, KU-57788: 249, Y-27632: 161 cells). Scale bar = 10μm. ***: *P*<0.001 and NS: not significant, Student's *t*-test.

**Figure 5. α-TAT1 has a C-terminal phospho-inhibited NLS.**

a) Cartoon showing α-TAT1 putative NLS flanked by potential phosphosites and corresponding mutants, b) intracellular distribution of mVenus-α-TAT1 mutants as indicated, nuclei are outlined in red dotted lines, c) ratiometric analysis (WT: 304, T322A: 228, ST/A: 194, delNLS: 208, NES/A, ST/A: 225 cells) and d) categorical analysis (WT: 1032, T322A: 346, ST/A: 290, delNLS: 563, NES/A, ST/A: 476 cells) of intracellular localization of mVenus-α-TAT1 mutants,

e) proposed model of α-TAT1 localization and its impact on microtubule acetylation. Scale bar = 10µm. ***$P$<0.001 and NS, not significant, Student's $t$-test.

## References:

1. L'Hernault, S. W. & Rosenbaum, J. L. Chlamydomonas alpha-tubulin is posttranslationally modified by acetylation on the epsilon-amino group of a lysine. *Biochemistry* **24**, 473–478 (1985).
2. Diggins, M. A. & Dove, W. F. Distribution of acetylated alpha-tubulin in Physarum polycephalum. *J. Cell Biol.* **104**, 303–309 (1987).
3. Janke, C. & Montagnac, G. Causes and Consequences of Microtubule Acetylation. *Curr. Biol.* **27**, R1287–R1292 (2017).
4. Schatten, G. *et al.* Acetylated alpha-tubulin in microtubules during mouse fertilization and early development. *Dev. Biol.* **130**, 74–86 (1988).
5. Boggs, A. E. *et al.* α-Tubulin Acetylation Elevated in Metastatic and Basal-like Breast Cancer Cells Promotes Microtentacle Formation, Adhesion, and Invasive Migration. *Cancer Res.* **75**, 203–215 (2015).
6. Esteves, A. R. *et al.* Acetylation as a major determinant to microtubule-dependent autophagy: Relevance to Alzheimer's and Parkinson disease pathology. *Biochim. Biophys. Acta BBA - Mol. Basis Dis.* **1865**, 2008–2023 (2019).
7. L'Hernault, S. W. & Rosenbaum, J. L. Chlamydomonas alpha-tubulin is posttranslationally modified in the flagella during flagellar assembly. *J. Cell Biol.* **97**, 258–263 (1983).
8. Maruta, H., Greer, K. & Rosenbaum, J. L. The acetylation of alpha-tubulin and its relationship to the assembly and disassembly of microtubules. *J. Cell Biol.* **103**, 571–579 (1986).
9. Piperno, G., LeDizet, M. & Chang, X. J. Microtubules containing acetylated alpha-tubulin in mammalian cells in culture. *J. Cell Biol.* **104**, 289–302 (1987).

10. Sudo, H. & Baas, P. W. Acetylation of Microtubules Influences Their Sensitivity to Severing by Katanin in Neurons and Fibroblasts. *J. Neurosci.* **30**, 7215–7226 (2010).
11. Portran, D., Schaedel, L., Xu, Z., Théry, M. & Nachury, M. V. Tubulin acetylation protects long-lived microtubules against mechanical ageing. *Nat. Cell Biol.* **19**, 391–398 (2017).
12. Xu, Z. *et al.* Microtubules acquire resistance from mechanical breakage through intralumenal acetylation. *Science* **356**, 328–332 (2017).
13. Eshun-Wilson, L. *et al.* Effects of α-tubulin acetylation on microtubule structure and stability. *Proc. Natl. Acad. Sci.* **116**, 10366–10371 (2019).
14. Joo, E. E. & Yamada, K. M. MYPT1 regulates contractility and microtubule acetylation to modulate integrin adhesions and matrix assembly. *Nat. Commun.* **5**, 3510 (2014).
15. Bance, B., Seetharaman, S., Leduc, C., Boëda, B. & Etienne-Manneville, S. Microtubule acetylation but not detyrosination promotes focal adhesion dynamics and astrocyte migration. *J. Cell Sci.* **132**, (2019).
16. Swiatlowska, P., Sanchez-Alonso, J. L., Wright, P. T., Novak, P. & Gorelik, J. Microtubules regulate cardiomyocyte transversal Young's modulus. *Proc. Natl. Acad. Sci.* **117**, 2764–2766 (2020).
17. Coleman, A. K., Joca, H. C., Shi, G., Lederer, W. J. & Ward, C. W. Tubulin acetylation increases cytoskeletal stiffness to regulate mechanotransduction in striated muscle. *bioRxiv* 2020.06.10.144931 (2020) doi:10.1101/2020.06.10.144931.
18. Zhang, Y. *et al.* Identification of genes expressed in C. elegans touch receptor neurons. *Nature* **418**, 331–335 (2002).
19. Shida, T., Cueva, J. G., Xu, Z., Goodman, M. B. & Nachury, M. V. The major α-tubulin K40 acetyltransferase αTAT1 promotes rapid ciliogenesis and efficient mechanosensation. *Proc. Natl. Acad. Sci. U. S. A.* **107**, 21517–21522 (2010).

20. Morley, S. J. *et al.* Acetylated tubulin is essential for touch sensation in mice. *eLife* **5**, e20813 (2016).
21. Yan, C. *et al.* Microtubule Acetylation Is Required for Mechanosensation in Drosophila. *Cell Rep.* **25**, 1051-1065.e6 (2018).
22. Lin, S., Sterling, N. A., Junker, I. P., Helm, C. T. & Smith, G. M. Effects of αTAT1 and HDAC5 on axonal regeneration in adult neurons. *PloS One* **12**, e0177496 (2017).
23. Fourcade, S. *et al.* Loss of SIRT2 leads to axonal degeneration and locomotor disability associated with redox and energy imbalance. *Aging Cell* **16**, 1404–1413 (2017).
24. Morelli, G. *et al.* p27Kip1 Modulates Axonal Transport by Regulating α-Tubulin Acetyltransferase 1 Stability. *Cell Rep.* **23**, 2429–2442 (2018).
25. Lee, C.-C., Cheng, Y.-C., Chang, C.-Y., Lin, C.-M. & Chang, J.-Y. Alpha-tubulin acetyltransferase/MEC-17 regulates cancer cell migration and invasion through epithelial–mesenchymal transition suppression and cell polarity disruption. *Sci. Rep.* **8**, 17477 (2018).
26. Castro-Castro, A., Janke, C., Montagnac, G., Paul-Gilloteaux, P. & Chavrier, P. ATAT1/MEC-17 acetyltransferase and HDAC6 deacetylase control a balance of acetylation of alpha-tubulin and cortactin and regulate MT1-MMP trafficking and breast tumor cell invasion. *Eur. J. Cell Biol.* **91**, 950–960 (2012).
27. Oh, S. *et al.* Genetic disruption of tubulin acetyltransferase, αTAT1, inhibits proliferation and invasion of colon cancer cells through decreases in Wnt1/β-catenin signaling. *Biochem. Biophys. Res. Commun.* **482**, 8–14 (2017).
28. Geeraert, C. *et al.* Starvation-induced Hyperacetylation of Tubulin Is Required for the Stimulation of Autophagy by Nutrient Deprivation. *J. Biol. Chem.* **285**, 24184–24194 (2010).

29. McLendon, P. M. *et al.* Tubulin hyperacetylation is adaptive in cardiac proteotoxicity by promoting autophagy. *Proc. Natl. Acad. Sci.* **111**, E5178–E5186 (2014).

30. Destaing, O. *et al.* A novel Rho-mDia2-HDAC6 pathway controls podosome patterning through microtubule acetylation in osteoclasts. *J. Cell Sci.* **118**, 2901–2911 (2005).

31. Elliott, G. & O'Hare, P. Herpes Simplex Virus Type 1 Tegument Protein VP22 Induces the Stabilization and Hyperacetylation of Microtubules. *J. Virol.* **72**, 6448–6455 (1998).

32. Husain, M. & Harrod, K. S. Enhanced acetylation of alpha-tubulin in influenza A virus infected epithelial cells. *FEBS Lett.* **585**, 128–132 (2011).

33. Sabo, Y. *et al.* HIV-1 induces the formation of stable microtubules to enhance early infection. *Cell Host Microbe* **14**, (2013).

34. Zan, J. *et al.* Rabies Virus Infection Induces Microtubule Depolymerization to Facilitate Viral RNA Synthesis by Upregulating HDAC6. *Front. Cell. Infect. Microbiol.* **7**, (2017).

35. Kalebic, N. *et al.* αTAT1 is the major α-tubulin acetyltransferase in mice. *Nat. Commun.* **4**, 1–10 (2013).

36. Kim, G.-W., Li, L., Ghorbani, M., You, L. & Yang, X.-J. Mice lacking α-tubulin acetyltransferase 1 are viable but display α-tubulin acetylation deficiency and dentate gyrus distortion. *J. Biol. Chem.* **288**, 20334–20350 (2013).

37. Szyk, A. *et al.* Molecular Basis for Age-Dependent Microtubule Acetylation by Tubulin Acetyltransferase. *Cell* **157**, 1405–1415 (2014).

38. Kalebic, N. *et al.* Tubulin Acetyltransferase αTAT1 Destabilizes Microtubules Independently of Its Acetylation Activity. *Mol. Cell. Biol.* **33**, 1114–1123 (2013).

39. Friedmann, D. R., Aguilar, A., Fan, J., Nachury, M. V. & Marmorstein, R. Structure of the α-tubulin acetyltransferase, αTAT1, and implications for tubulin-specific acetylation. *Proc. Natl. Acad. Sci. U. S. A.* **109**, 19655–19660 (2012).

40. Mészáros, B., Erdős, G. & Dosztányi, Z. IUPred2A: context-dependent prediction of protein disorder as a function of redox state and protein binding. *Nucleic Acids Res.* **46**, W329–W337 (2018).
41. Ishida, T. & Kinoshita, K. PrDOS: prediction of disordered protein regions from amino acid sequence. *Nucleic Acids Res.* **35**, W460-464 (2007).
42. la Cour, T. *et al.* Analysis and prediction of leucine-rich nuclear export signals. *Protein Eng. Des. Sel.* **17**, 527–536 (2004).
43. Horton, P. *et al.* WoLF PSORT: protein localization predictor. *Nucleic Acids Res.* **35**, W585-587 (2007).
44. Kosugi, S. *et al.* Six Classes of Nuclear Localization Signals Specific to Different Binding Grooves of Importin α. *J. Biol. Chem.* **284**, 478–485 (2009).
45. Kutay, U. & Güttinger, S. Leucine-rich nuclear-export signals: born to be weak. *Trends Cell Biol.* **15**, 121–124 (2005).
46. Hutten, S. & Kehlenbach, R. H. CRM1-mediated nuclear export: to the pore and beyond. *Trends Cell Biol.* **17**, 193–201 (2007).
47. Sun, Q. *et al.* Nuclear export inhibition through covalent conjugation and hydrolysis of Leptomycin B by CRM1. *Proc. Natl. Acad. Sci.* **110**, 1303–1308 (2013).
48. Sekimoto, T., Fukumoto, M. & Yoneda, Y. 14-3-3 suppresses the nuclear localization of threonine 157-phosphorylated p27Kip1. *EMBO J.* **23**, 1934–1942 (2004).
49. Mancini, M. *et al.* 14-3-3 ligand prevents nuclear import of c-ABL protein in chronic myeloid leukemia. *Traffic Cph. Den.* **10**, 637–647 (2009).
50. Huang, X. *et al.* Shade-induced nuclear localization of PIF7 is regulated by phosphorylation and 14-3-3 proteins in Arabidopsis. *eLife* **7**, (2018).
51. Yaffe, M. B. *et al.* The Structural Basis for 14-3-3:Phosphopeptide Binding Specificity. *Cell* **91**, 961–971 (1997).

52. Madeira, F. *et al.* 14-3-3-Pred: improved methods to predict 14-3-3-binding phosphopeptides. *Bioinforma. Oxf. Engl.* **31**, 2276–2283 (2015).
53. Seetharaman, S. *et al.* Microtubules tune mechanosensitive cell responses. *bioRxiv* 2020.07.22.205203 (2020) doi:10.1101/2020.07.22.205203.
54. Vassilev, L. T. *et al.* Selective small-molecule inhibitor reveals critical mitotic functions of human CDK1. *Proc. Natl. Acad. Sci. U. S. A.* **103**, 10660–10665 (2006).
55. Jorda, R. *et al.* How Selective Are Pharmacological Inhibitors of Cell-Cycle-Regulating Cyclin-Dependent Kinases? *J. Med. Chem.* **61**, 9105–9120 (2018).
56. Fry, D. W. *et al.* Specific inhibition of cyclin-dependent kinase 4/6 by PD 0332991 and associated antitumor activity in human tumor xenografts. *Mol. Cancer Ther.* **3**, 1427–1438 (2004).
57. Toogood, P. L. *et al.* Discovery of a Potent and Selective Inhibitor of Cyclin-Dependent Kinase 4/6. *J. Med. Chem.* **48**, 2388–2406 (2005).
58. Ferguson, A. D. *et al.* Structural basis of CX-4945 binding to human protein kinase CK2. *FEBS Lett.* **585**, 104–110 (2011).
59. Rena, G., Bain, J., Elliott, M. & Cohen, P. D4476, a cell-permeant inhibitor of CK1, suppresses the site-specific phosphorylation and nuclear exclusion of FOXO1a. *EMBO Rep.* **5**, 60–65 (2004).
60. Kim, A. K., Wu, H. D. & Inoue, T. Rational Design of a Protein Kinase A Nuclear-cytosol Translocation Reporter. *Sci. Rep.* **10**, 9365 (2020).
61. Harreman, M. T. *et al.* Regulation of nuclear import by phosphorylation adjacent to nuclear localization signals. *J. Biol. Chem.* **279**, 20613–20621 (2004).
62. Shah, N. *et al.* TAK1 activation of alpha-TAT1 and microtubule hyperacetylation control AKT signaling and cell growth. *Nat. Commun.* **9**, 1–12 (2018).

63. Shimada, Y., Gulli, M. P. & Peter, M. Nuclear sequestration of the exchange factor Cdc24 by Far1 regulates cell polarity during yeast mating. *Nat. Cell Biol.* **2**, 117–124 (2000).

64. Volmat, V., Camps, M., Arkinstall, S., Pouysségur, J. & Lenormand, P. The nucleus, a site for signal termination by sequestration and inactivation of p42/p44 MAP kinases. *J. Cell Sci.* **114**, 3433–3443 (2001).

65. Formstecher, E. *et al.* PEA-15 mediates cytoplasmic sequestration of ERK MAP kinase. *Dev. Cell* **1**, 239–250 (2001).

66. Yang, W., Wightman, R. & Meyerowitz, E. M. Cell Cycle Control by Nuclear Sequestration of CDC20 and CDH1 mRNA in Plant Stem Cells. *Mol. Cell* **68**, 1108-1119.e3 (2017).

67. Lasker, K. *et al.* Selective sequestration of signalling proteins in a membraneless organelle reinforces the spatial regulation of asymmetry in Caulobacter crescentus. *Nat. Microbiol.* **5**, 418–429 (2020).

68. Chen, Y. *et al.* Aberrant subcellular localization of BRCA1 in breast cancer. *Science* **270**, 789–791 (1995).

69. Jiao, W. *et al.* Aberrant nucleocytoplasmic localization of the retinoblastoma tumor suppressor protein in human cancer correlates with moderate/poor tumor differentiation. *Oncogene* **27**, 3156–3164 (2008).

70. Hung, M.-C. & Link, W. Protein localization in disease and therapy. *J. Cell Sci.* **124**, 3381–3392 (2011).

71. Wang, X. & Li, S. Protein mislocalization: mechanisms, functions and clinical applications in cancer. *Biochim. Biophys. Acta* **1846**, 13–25 (2014).

72. Nekooki-Machida, Y. *et al.* Dynamic localization of α-tubulin acetyltransferase ATAT1 through the cell cycle in human fibroblastic KD cells. *Med. Mol. Morphol.* **51**, 217–226 (2018).

73. Pennington, K. L., Chan, T. Y., Torres, M. P. & Andersen, J. L. The dynamic and stress-adaptive signaling hub of 14-3-3: emerging mechanisms of regulation and context-dependent protein–protein interactions. *Oncogene* **37**, 5587–5604 (2018).

74. Yaffe, M. B. How do 14-3-3 proteins work?-- Gatekeeper phosphorylation and the molecular anvil hypothesis. *FEBS Lett.* **513**, 53–57 (2002).

75. Oeckinghaus, A. & Ghosh, S. The NF-κB Family of Transcription Factors and Its Regulation. *Cold Spring Harb. Perspect. Biol.* **1**, (2009).

76. Spencer, S. L. *et al.* The Proliferation-Quiescence Decision Is Controlled by a Bifurcation in CDK2 Activity at Mitotic Exit. *Cell* **155**, 369–383 (2013).

77. Regot, S., Hughey, J. J., Bajar, B. T., Carrasco, S. & Covert, M. W. High-Sensitivity Measurements of Multiple Kinase Activities in Live Single Cells. *Cell* **157**, 1724–1734 (2014).

78. Deneke, V. E., Melbinger, A., Vergassola, M. & Di Talia, S. Waves of Cdk1 activity in S-phase synchronize the cell cycle in Drosophila embryos. *Dev. Cell* **38**, 399–412 (2016).

79. Uchida, S. *et al.* Binding of 14-3-3β but not 14-3-3σ controls the cytoplasmic localization of CDC25B: binding site preferences of 14-3-3 subtypes and the subcellular localization of CDC25B. *J. Cell Sci.* **117**, 3011–3020 (2004).

80. Choudhary, C. *et al.* Lysine acetylation targets protein complexes and co-regulates major cellular functions. *Science* **325**, 834–840 (2009).

81. Andersen, J. L. *et al.* A biotin switch-based proteomics approach identifies 14-3-3ζ as a target of Sirt1 in the metabolic regulation of caspase-2. *Mol. Cell* **43**, 834–842 (2011).

82. Wright, P. E. & Dyson, H. J. Intrinsically Disordered Proteins in Cellular Signaling and Regulation. *Nat. Rev. Mol. Cell Biol.* **16**, 18–29 (2015).

83. Tate, J. G. *et al.* COSMIC: the Catalogue Of Somatic Mutations In Cancer. *Nucleic Acids Res.* **47**, D941–D947 (2019).

84. F, M. *et al.* The EMBL-EBI search and sequence analysis tools APIs in 2019. *Nucleic Acids Res.* **47**, W636–W641 (2019).

# Figure 1

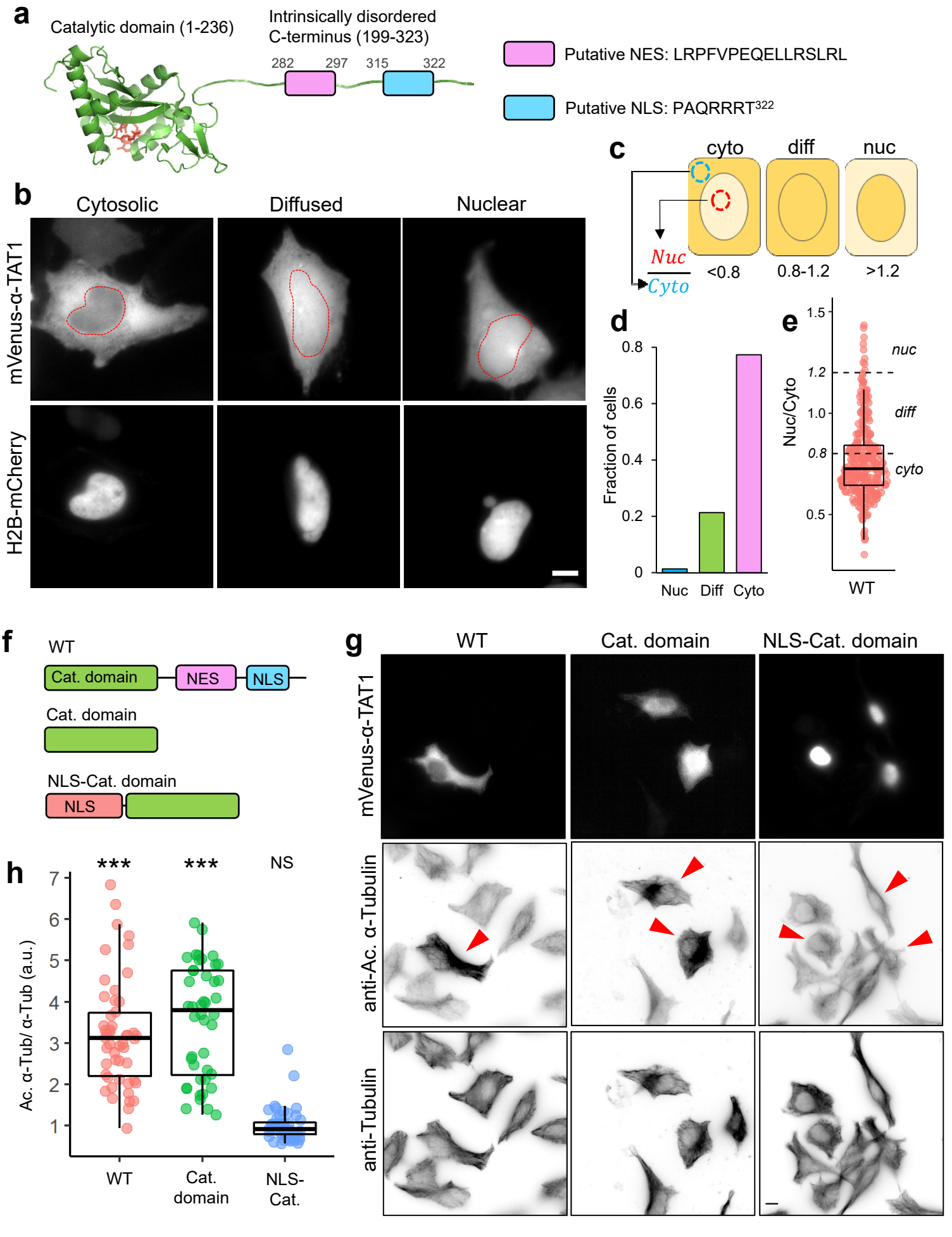

# Figure 2

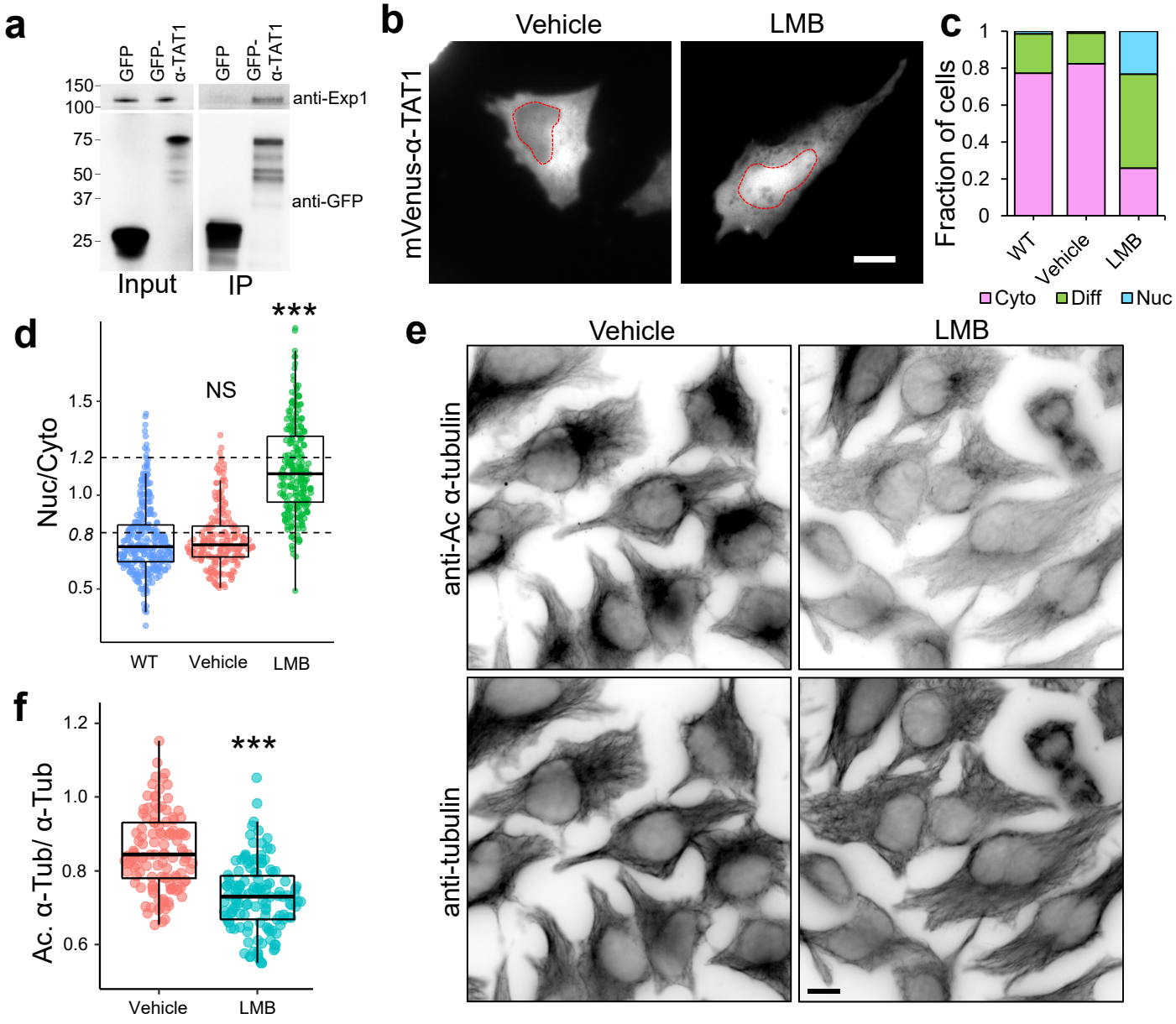

# Figure 3

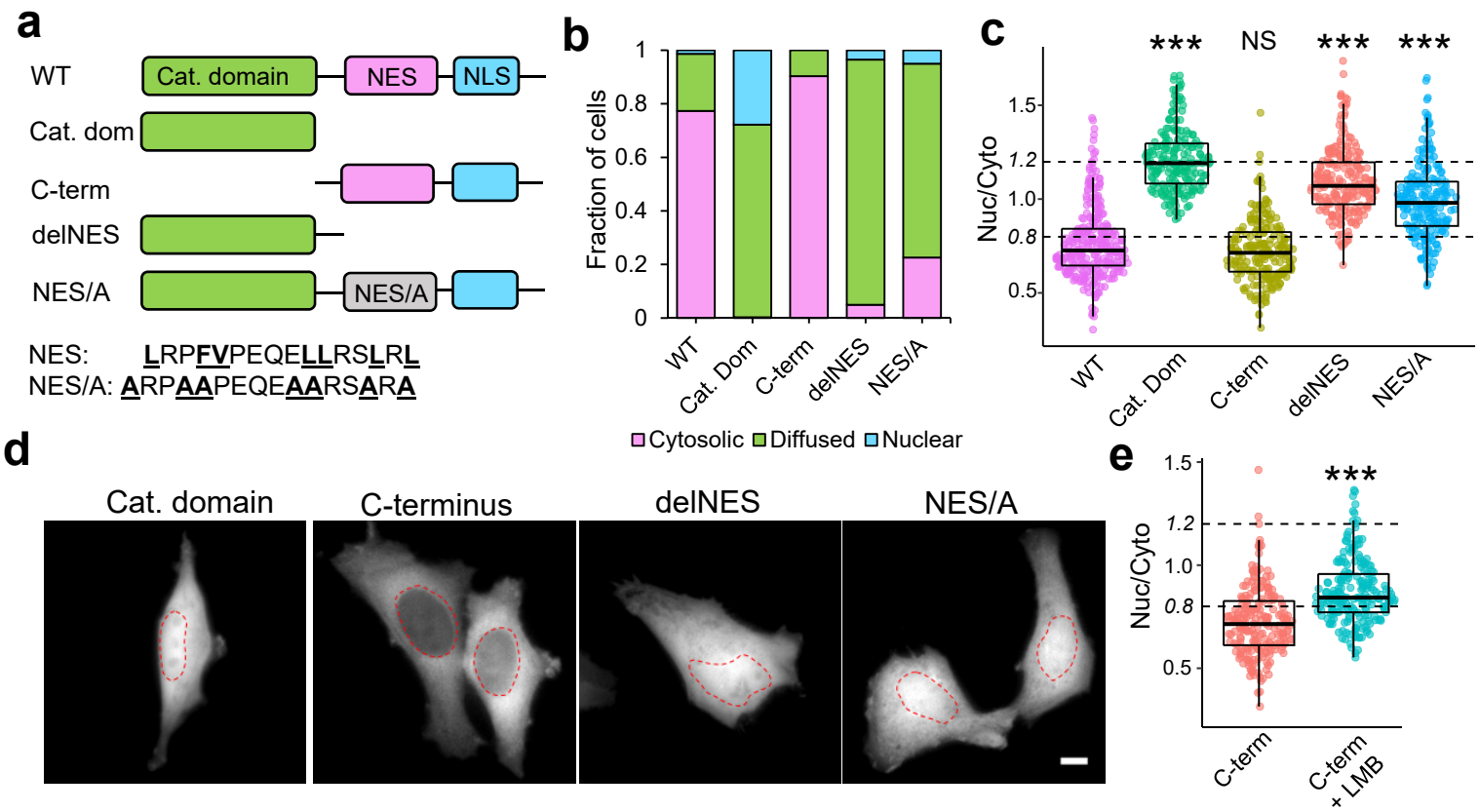

# Figure 4

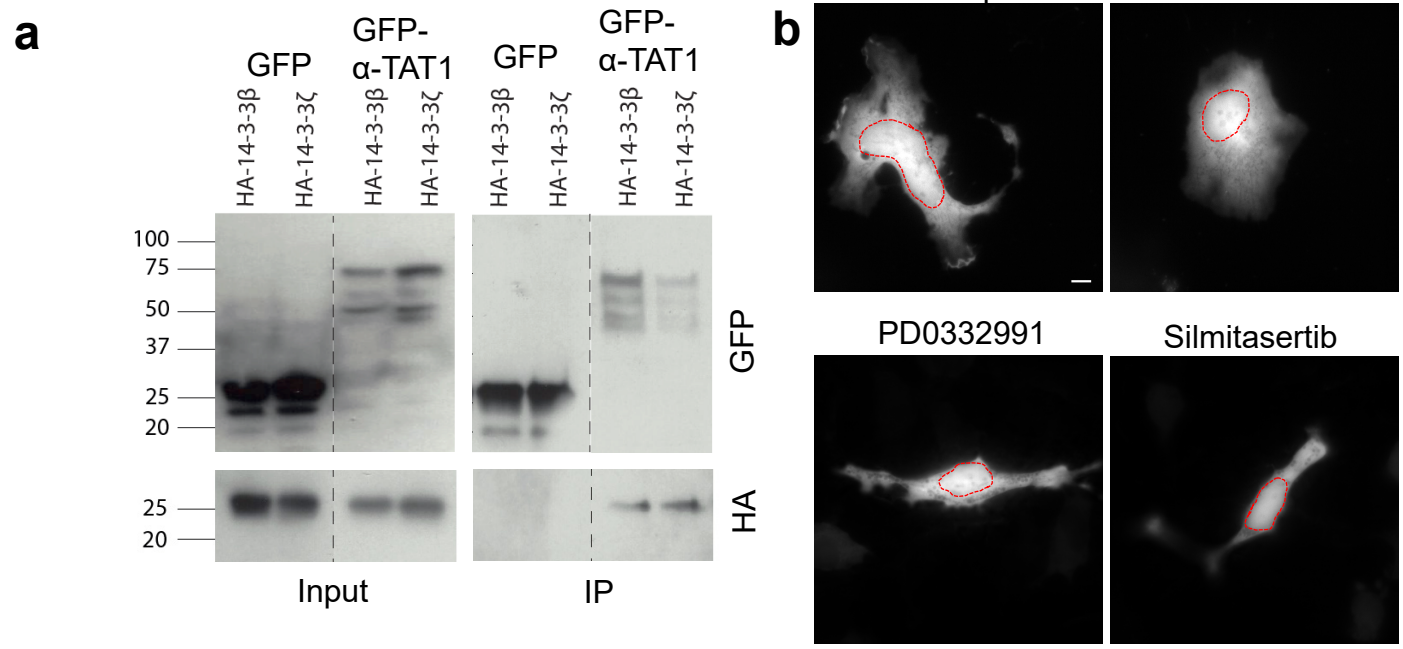


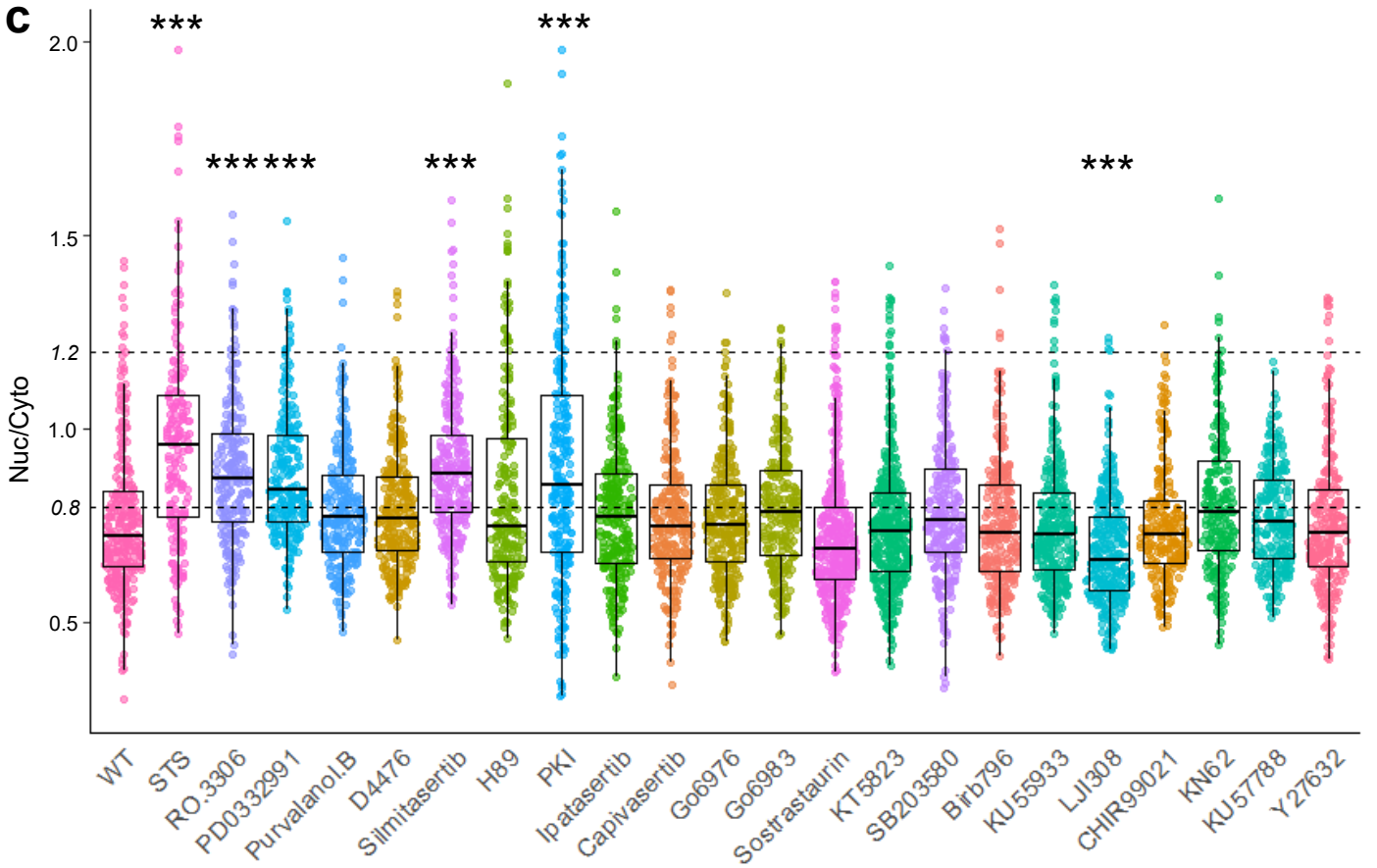

# Figure 5

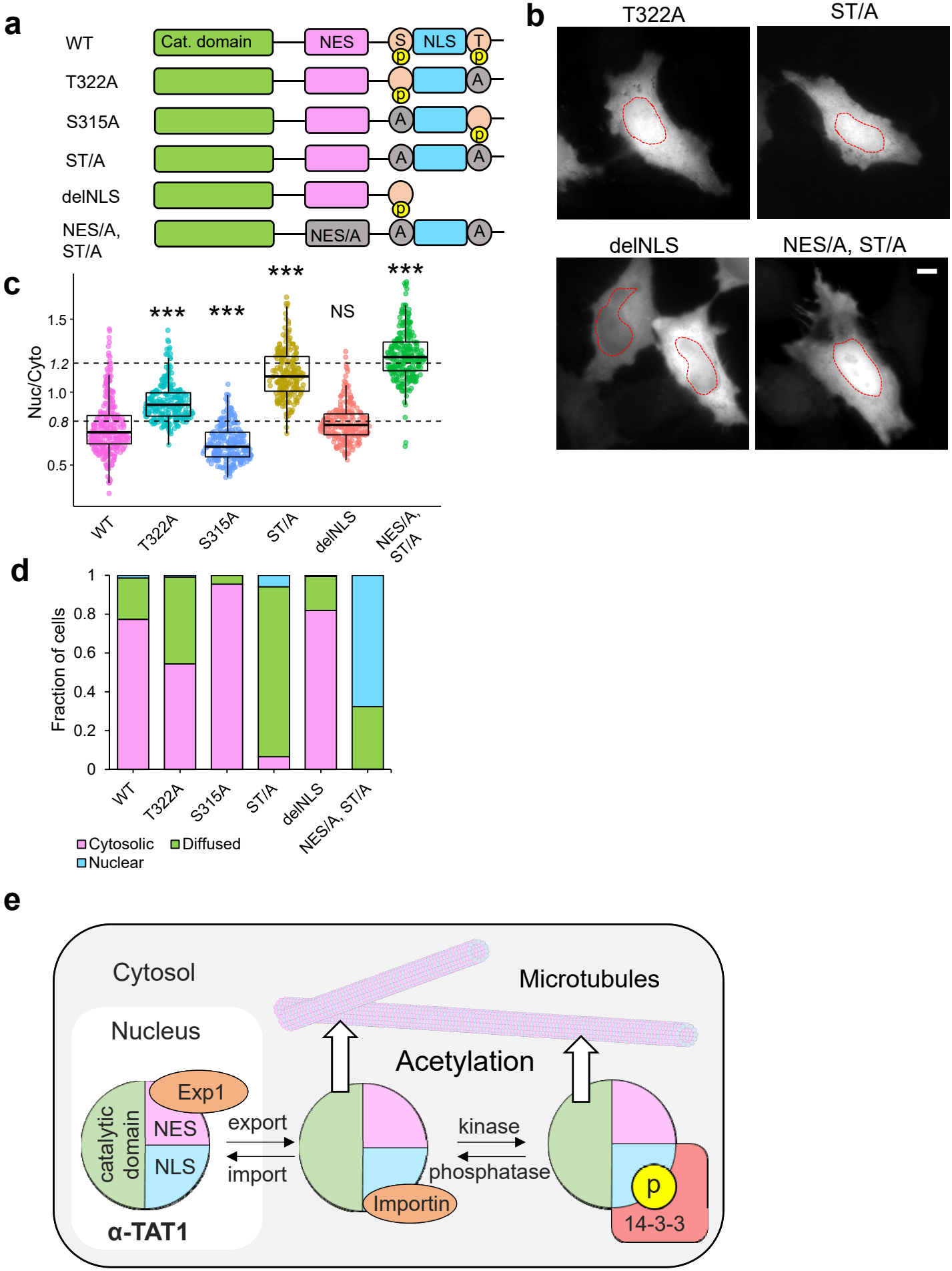

# Supplementary Information

## A phospho-regulated signal motif of α-TAT1 drives dynamic microtubule acetylation

Abhijit Deb Roy[1*], Evan G. Gross[2], Gayatri S. Pillai[2], Shailaja Seetharaman[3,4], Sandrine Etienne-Manneville[3], Takanari Inoue[1*]

[1] Department of Cell Biology and Center for Cell Dynamics, Johns Hopkins University School of Medicine, Baltimore, 855 North Wolfe Street, MD 21205, USA

[2] The Johns Hopkins University, Baltimore, MD 21218, USA

[3]Cell Polarity, Migration and Cancer Unit, Institut Pasteur, UMR3691 CNRS, Equipe Labellisée Ligue Contre le Cancer, F-75015, Paris, France.

[4]Université Paris Descartes, Sorbonne Paris Cité, 12 Rue de l'École de Médecine, 75006 Paris, France.

[*] Correspondence:
Abhijit Deb Roy abhijit.debroy@gmail.com
Takanari Inoue jctinoue@jhmi.edu

a) Query: α-TAT1 Isoform 7

MEFPFDVDALFPERITVLDQHLRPPARRPGTTTPARVDLQQQIMTIIDELGKASAKAQNLSAPITSA
SRMQSNRHVVYILKDSSARPAGKGAIIGFIKVGYKKLFVLDDREAHNEVEPLCILDFYIHESVQRH
GHGRELFQYMLQKERVEPHQLAIDRPSQKLLKFLNKHYNLETTVPQVNNFVIFEGFFAHQHRPPA
PSLRATRHSRAAAVDPTPAAPARKLPPKRAEGDIKPYSSSDREFLKVAVEPPWPLNRAPRRATP
PAHPPPRSSSLGNSPERGP**LRPFVPEQELLRSLRL**CPPHPTARLLLAADPGGS**PAQRRRT**[322]R

b)

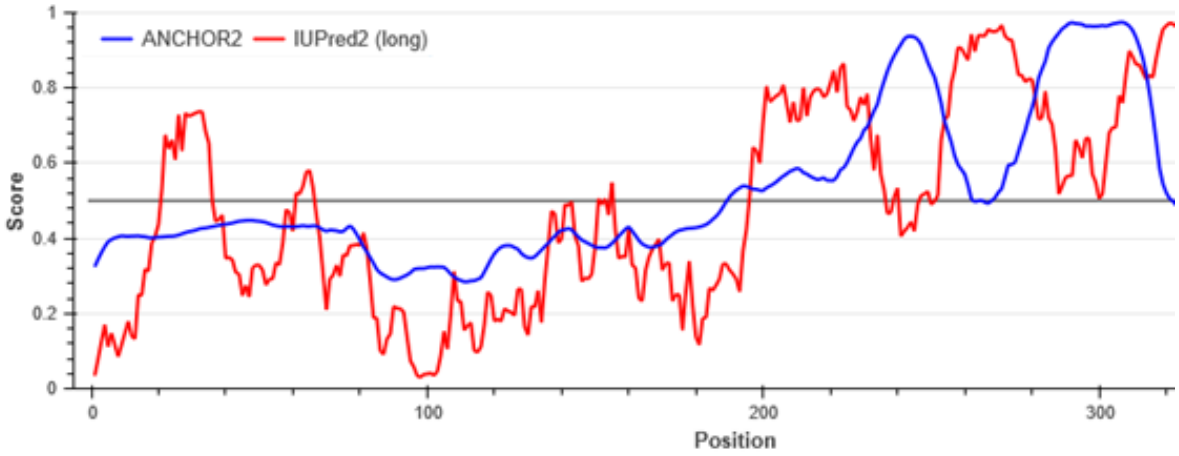


c)

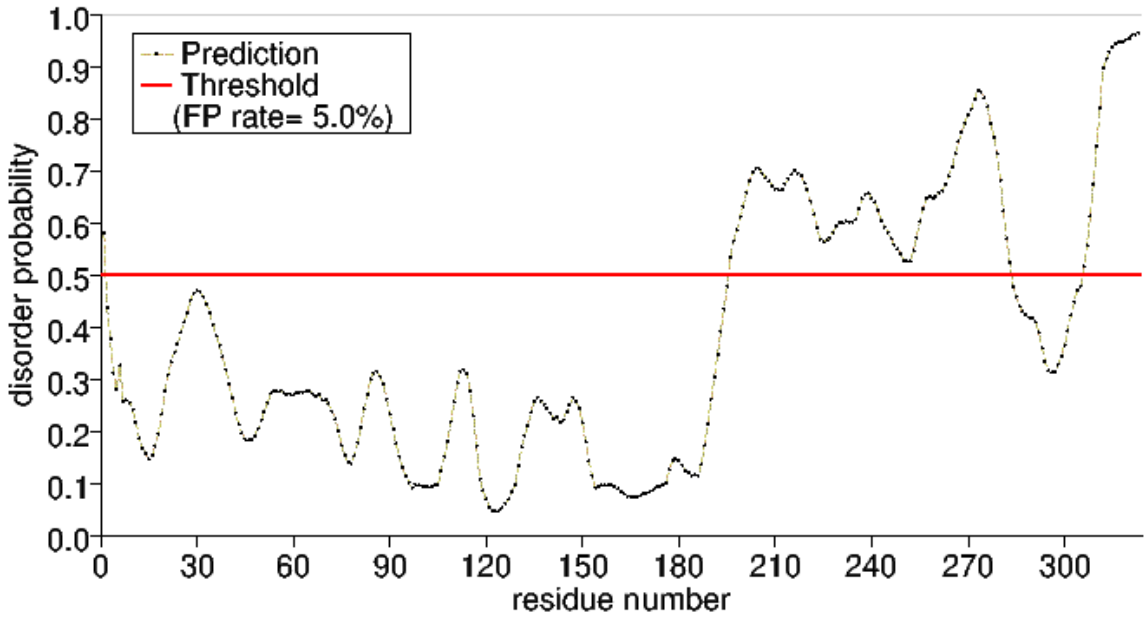


**Supplementary Figure S1.** αTAT1 C-terminus is disordered. a) amino acid sequence of αTAT1 isoform 7 used as the query, the putative NES and NLS are in bold, b) IUPred2 (and ANCHOR2) and c) PrDOS results suggesting that αTAT1 C-terminus is disordered. The threshold to be considered disordered is 0.5 for both.

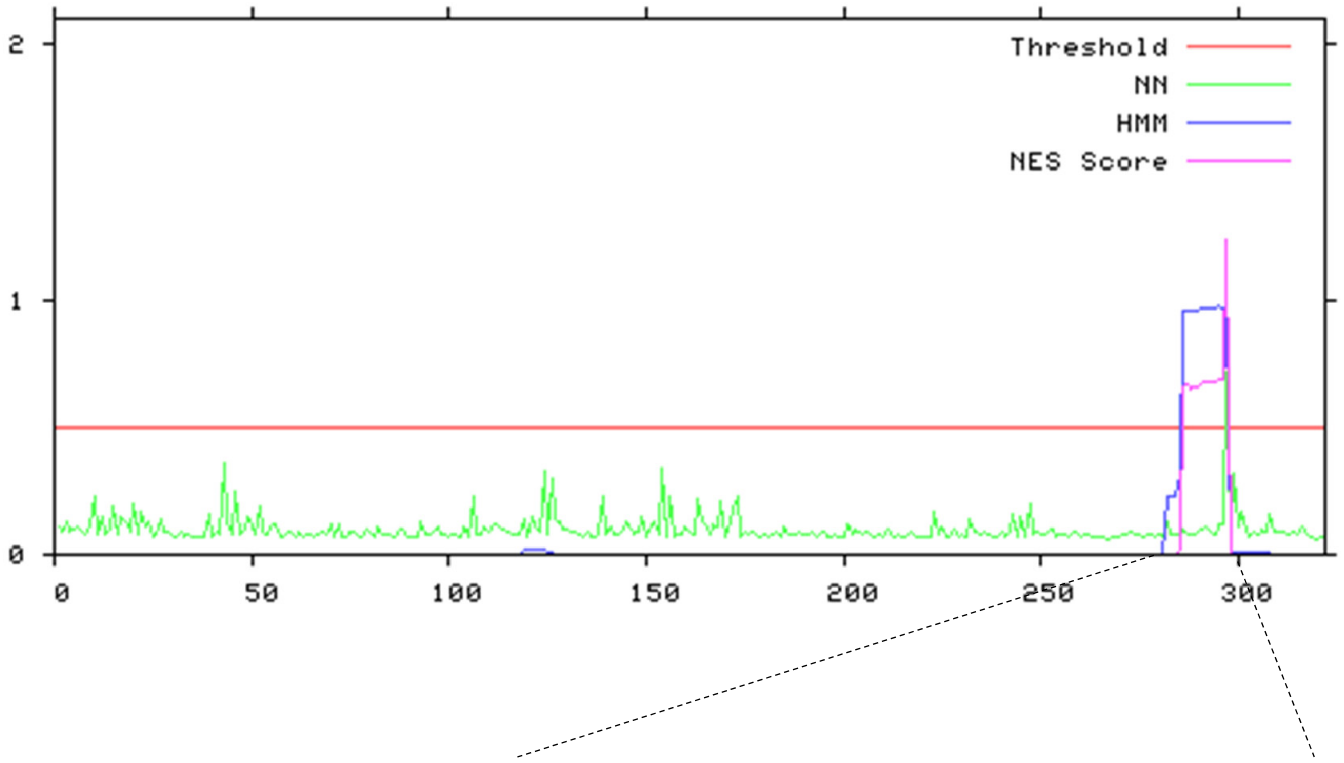


NetNES optimized prediction: LRPF**V**PEQE**LL**RS**L**R**L**

Hidden Makov Model (HMM) algorithm prediction: **L**RP**FV**PEQE**LL**RS**L**R**L**

**Supplementary Figure S2.** NetNES prediction for NES in αTAT1 identifying the putative NES, the predicted NES from NetNES optimized algorithm (pink) and that from Hidden Markov Model (blue) are shown with the hydrophobic residues indicated in bold.

a)

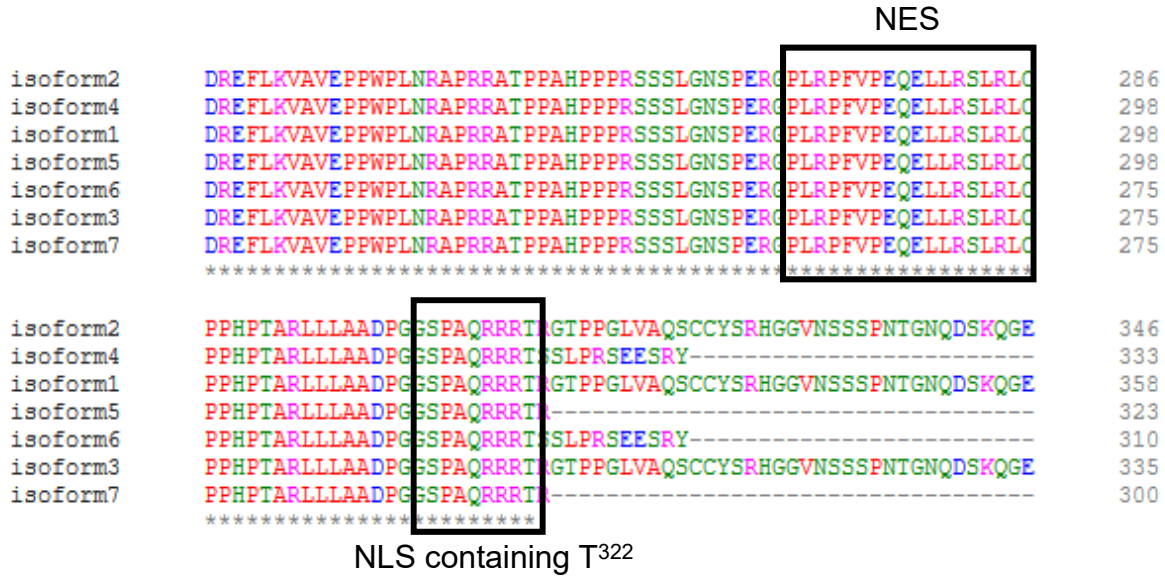


b)

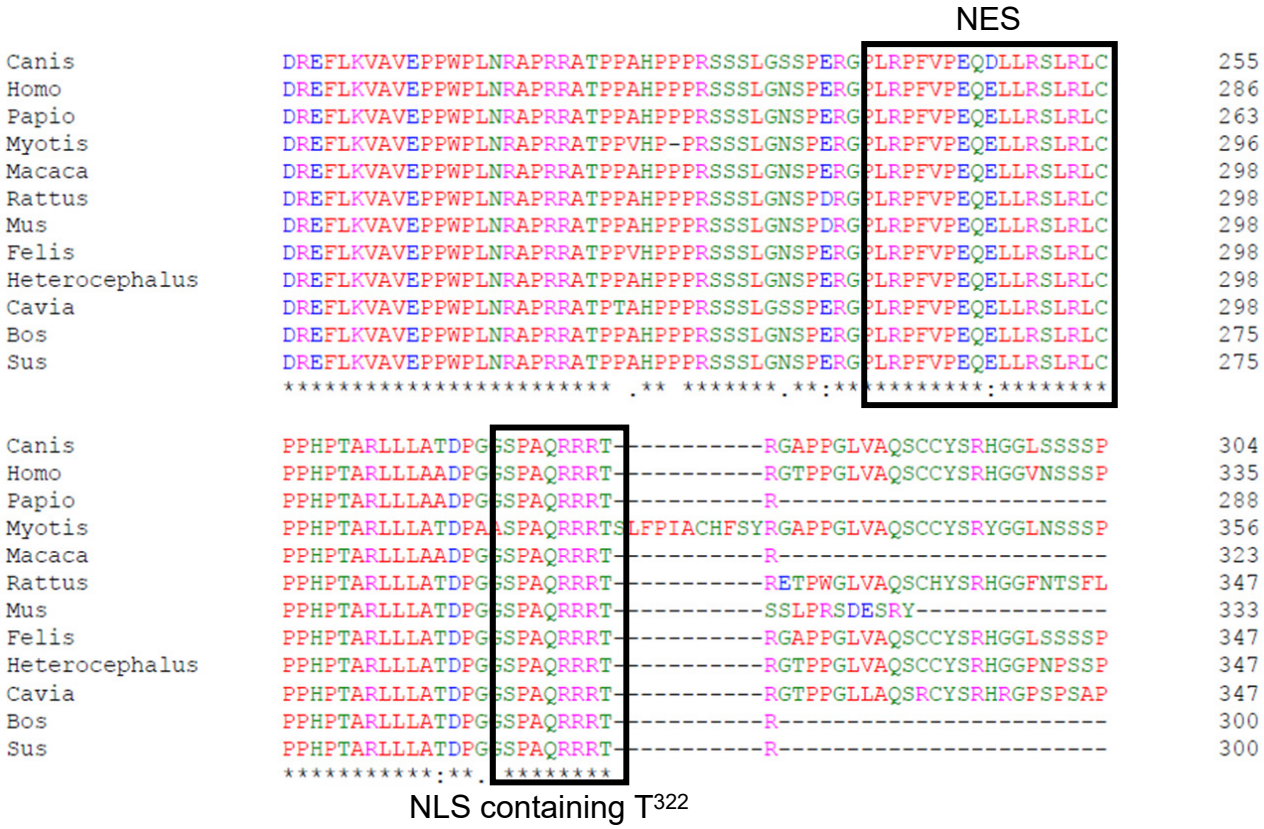


**Supplementary Figure S3.** The putative NES and NLS in α-TAT1 are evolutionarily conserved. a) Alignment of human α-TAT1 isoforms, b) alignment of different mammalian α-TAT1 showing the C-terminal region including the putative NES and NLS (enclosed in boxes), genus of the mammalian α-TAT1 are shown. Alignments were performed using ClustalW (https://www.ebi.ac.uk/Tools/msa/clustalo/)

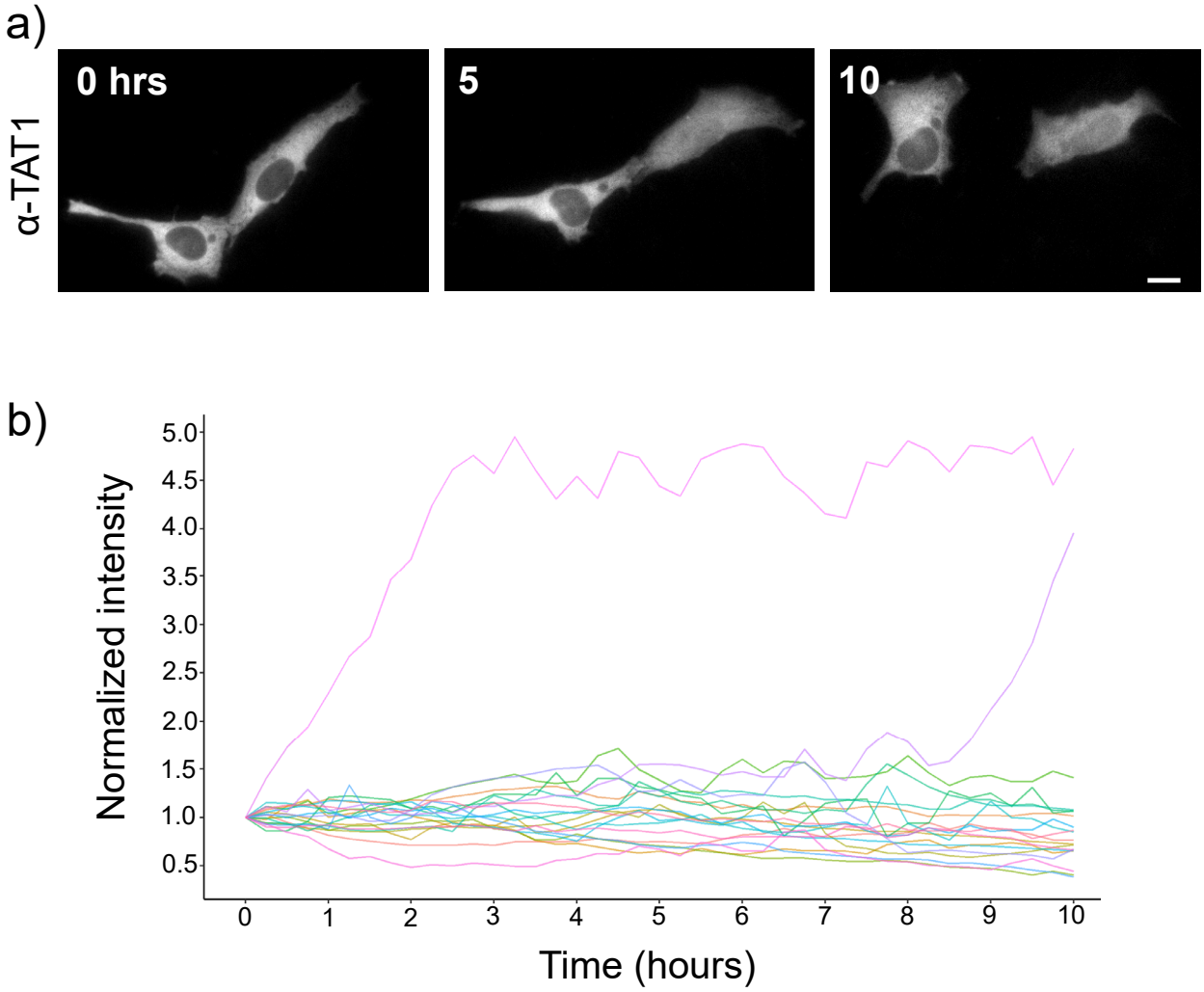


**Supplementary Figure S4.** α-TAT1 intracellular localization is dynamic in nature. a) Spontaneous temporal changes in spatial distribution of mVenus-α-TAT1, scale bar = 10 μm b) temporal changes in nuclear fluorescence intensity of mVenus-α-TAT1 in HeLa cells, each line indicates normalized nuclear intensity of mVenus- α-TAT1 in a single cell, n = 20 cells

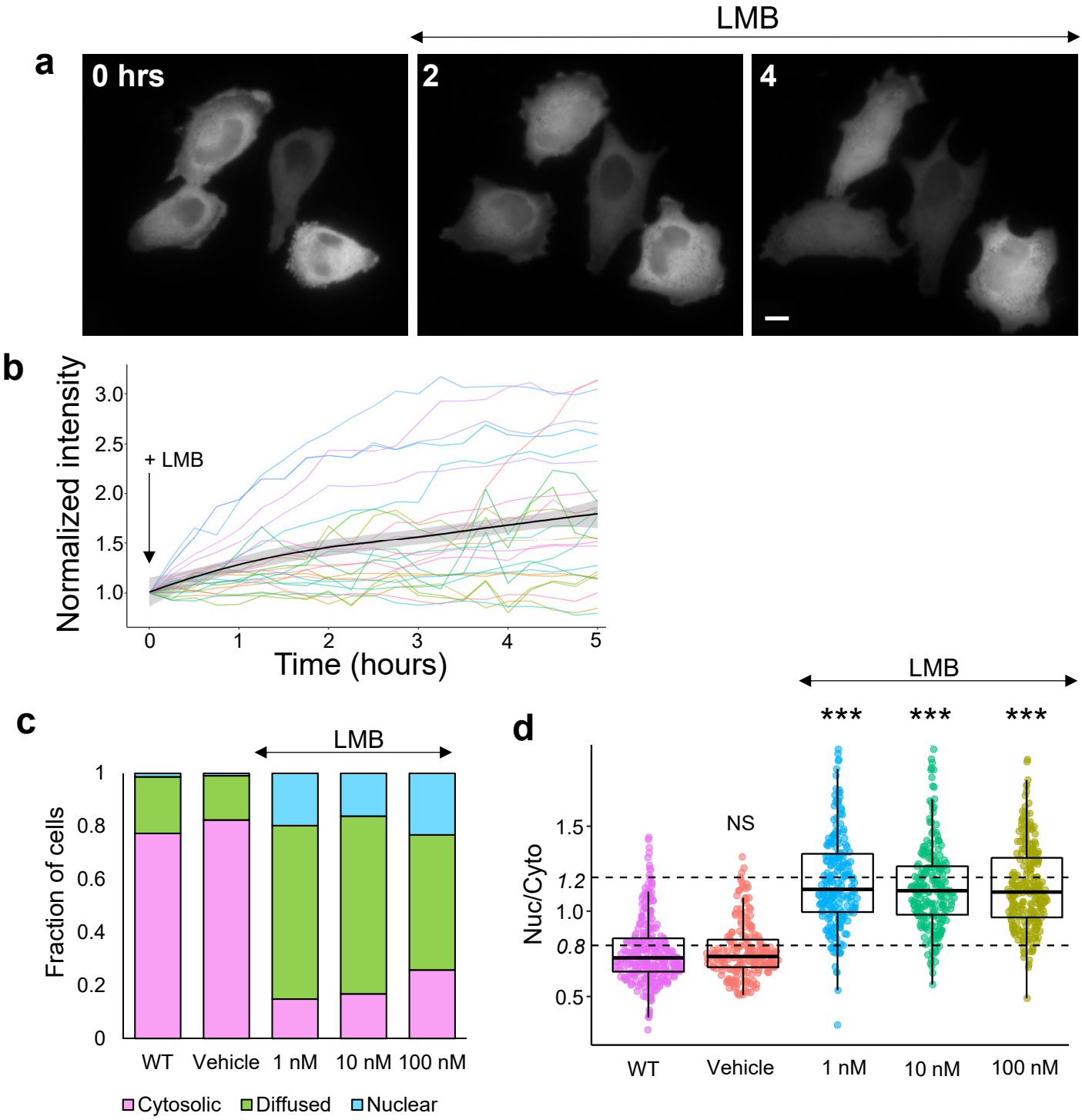


**Supplementary Figure S5.** α-TAT1 undergoes CRM1 dependent nuclear export. a), b) Temporal changes in mVenus-α-TAT1 localization on 100 nM LMB treatment after LMB addition at time 0, scale bar = 10 μm, for b), each line indicates normalized nuclear intensity of mVenus- α-TAT1 in a single cell, black line shows the mean and gray line indicate the 95% C.I., n = 26 cells , c) categorical analysis (WT: 1032, vehicle: 450, 1 nM: 329, 10 nM: 291, 100 nM: 495 cells) and d) ratiometric analysis (WT: 304, vehicle: 210, 1 nM: 203, 10 nM: 200, 100 nM: 240 cells) of mVenus-α-TAT1 localization on vehicle (EtOH) or LMB treatment at 1, 10 and 100 nM. ***$P$<0.001 and NS, not significant, Student's $t$-test.

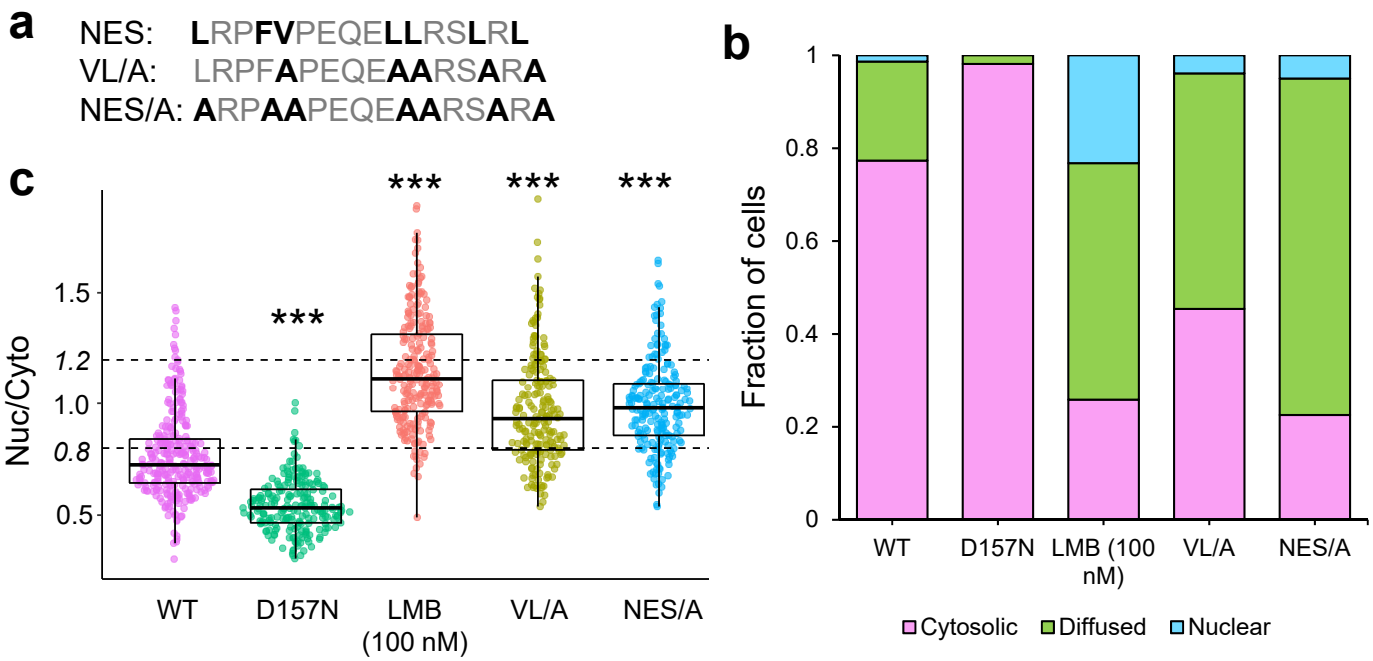


**Supplementary Figure S6.** α-TAT1 has a C-terminal NES. a) α-TAT1 NES predicted by NetNES and mutants using alanine substitution, b) categorical (WT: 1032, D157N: 429, LMB: 495, VL/A: 436, NES/A: 501 cells), and c) ratiometric (WT: 304, D157N: 217, LMB: 240, VL/A: 201, NES/A: 212 cells) analyses of intracellular localization of mVenus-α-TAT1 and mutants as indicated. ***$P$<0.001 and NS, not significant, Student's $t$-test.

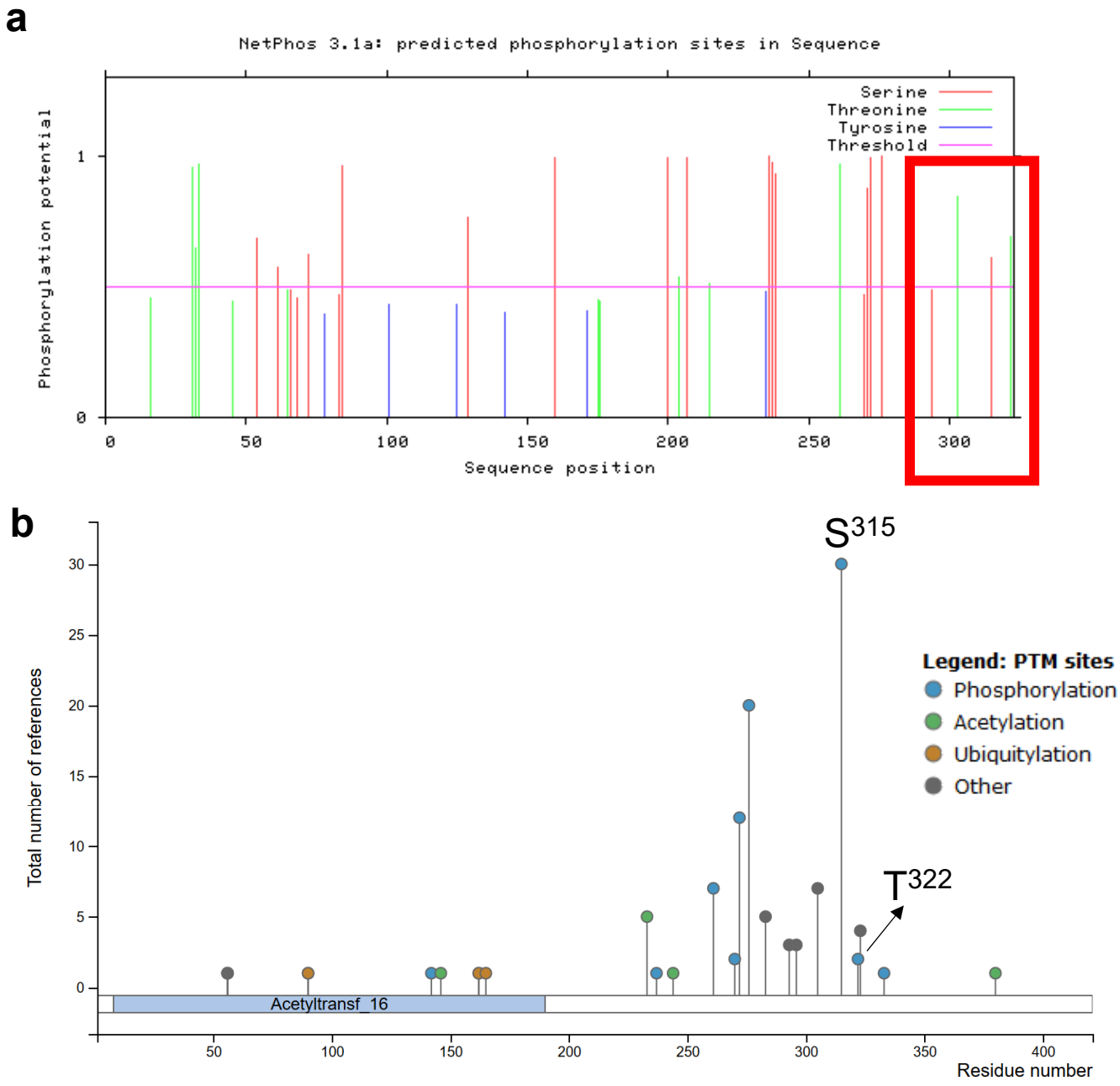


**Supplementary Figure S7.** a) Putative phosphosites in α-TAT1 predicted by NetPhos, those in F285-R323 are highlighted, b) currently reported post-translational modifications in α-TAT1 curated by PhosphoSitePlus®, www.phosphosite.org.

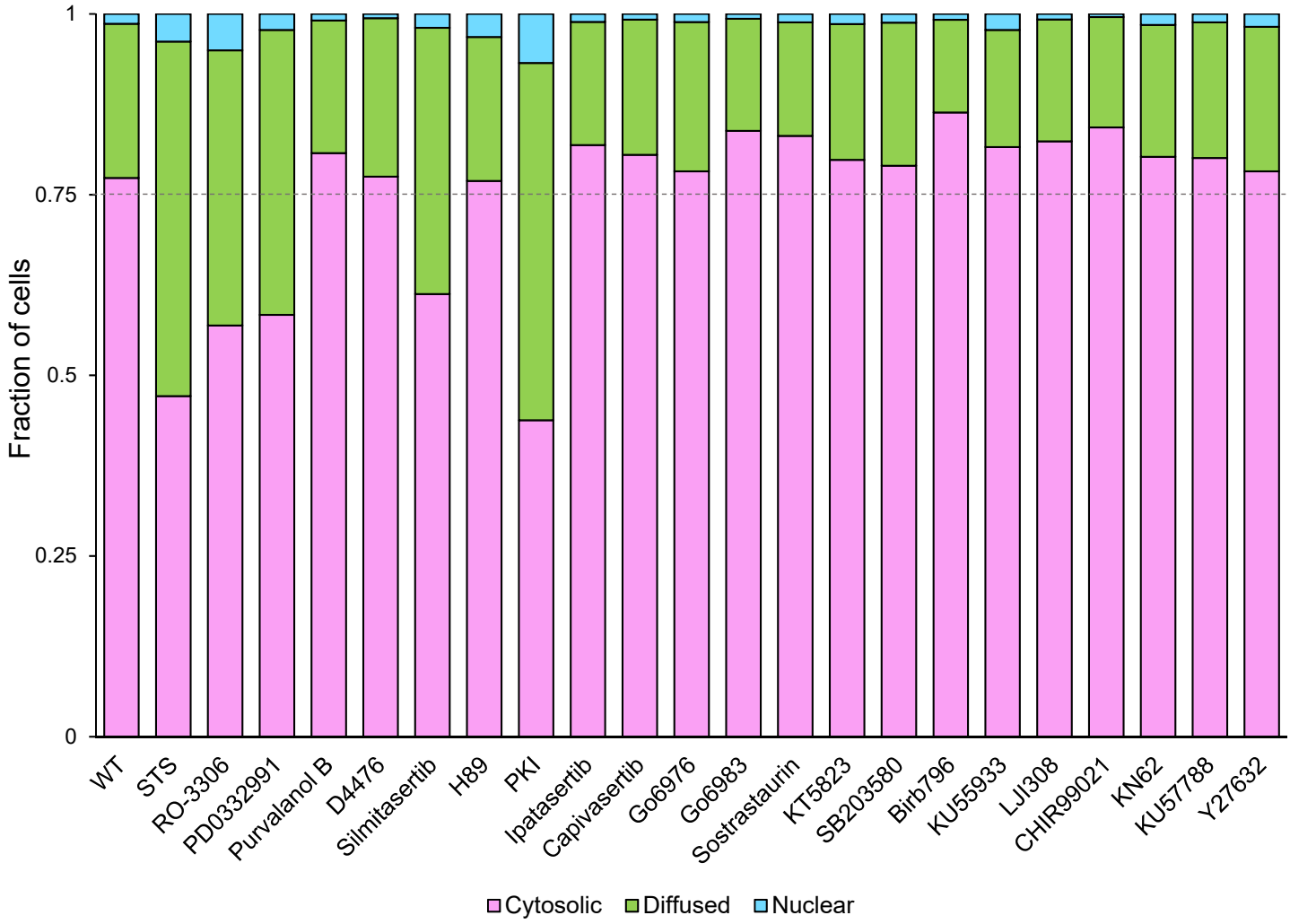


**Supplementary Figure S8.** Categorical analysis of α-TAT1 localization on treatment with kinase inhibitors. WT: 1032, STS: 157, R0-3306: 796, PD0332991: 543, Purvalanol B: 992, D4476: 689, 418, H89: 251, PKI: 354, Ipatasertib: 546, Capivasertib: 385, Go6976: 712, Go6983: 606, Sostrastaurin: 605, KT5823: 570, SB203580: 505, Birb796: 991, KU55933: 815, LJI308: 522, CHIR99021: 484, KN62: 531, KU57788: 949, Y27632: 340 cells.

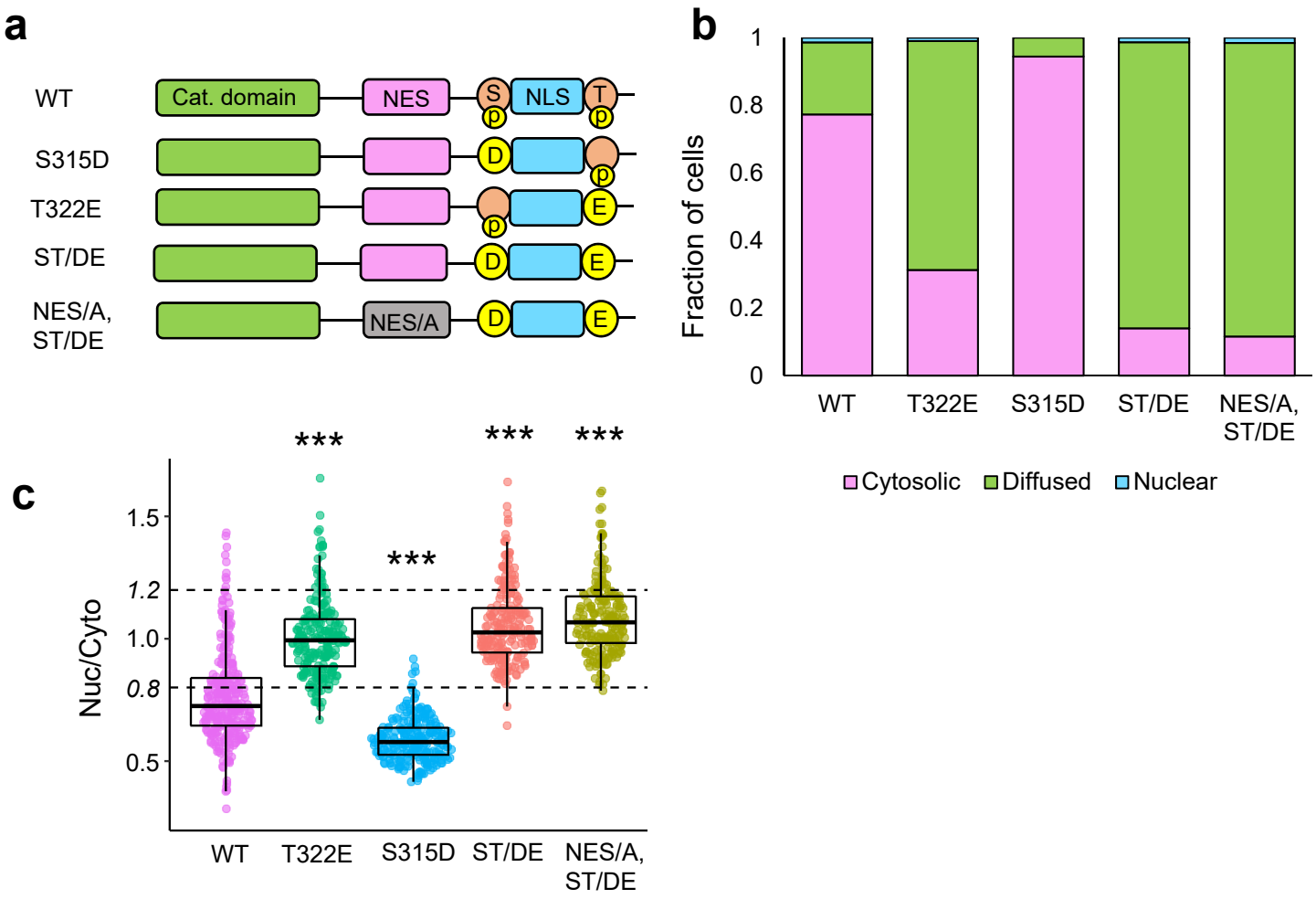


**Supplementary Figure S9.** α-TAT1 has a C-terminal phospho-inhibited NLS. a) Cartoon showing α-TAT1 NES and NLS flanked by potential phosphosites and mutants, b) categorical (WT:1032, S315A: 442, S315D: 412, T322E: 310, ST/DE: 258 cells) and c) ratiometric (WT: 304, S315A: 212, S315D: 223, T322E: 232, ST/DE: 195 cells) analyses of intracellular localization of mVenus-α-TAT1 mutants. ***$P$<0.001 and NS, not significant, Student's $t$-test.

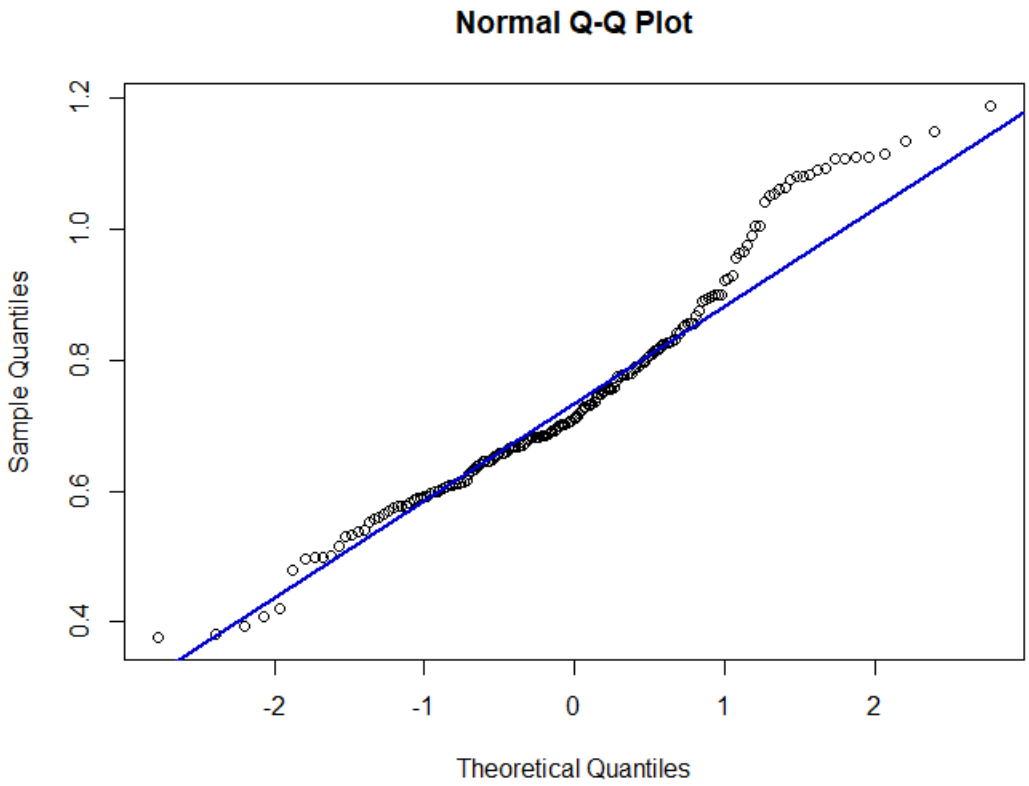


**Supplementary Figure S10.** Normal probability plot of nuclear/cytosolic ratio of mVenus-α-TAT1 expressed in HeLa cells.

| Drug | Conc. Used | target kinase | Incubation time | p value (t-test) |
|---|---|---|---|---|
| STS | 100 nM | Pan kinase | 4 hours | 1.20187E-11 |
| RO3306 | 10 μM | Cdk1, Cdk2 | 4 hours | 1.87845E-10 |
| PD0332991 | 1 μM | Cdk4, Cdk6 | 4 hours | 1.29985E-10 |
| Purvalanol B | 1 μM | Cdk1, Cdk2, Cdk5 | 4 hours | 0.086698844 |
| D4476 | 1 μM | CK1 | 4 hours | 0.244864719 |
| Silmitasertib | 10 μM | CK2 | 4 hours | 7.34743E-12 |
| H89 | 10 μM | PKA | 4 hours | 0.001868139 |
| PKI | NA | PKA | Overnight | 8.76993E-08 |
| Ipatasertib | 10 μM | PKB (Akt) | 4 hours | 0.026614985 |
| Capivasertib | 1 μM | PKB (Akt) | 4 hours | 0.928873535 |
| Go6976 | 250 nM | PKC | 4 hours | 0.900843024 |
| Go6983 | 250 nM | PKC | 4 hours | 0.068144954 |
| Sostrastaurin | 10 μM | PKC | 4 hours | 0.008916116 |
| KT5823 | 5 μM | PKG | 4 hours | 0.581314971 |
| SB203580 | 10 μM | p38 MAPK | 4 hours | 0.007945499 |
| Birb796 | 10 μM | p38 MAPK | 4 hours | 0.768174955 |
| KU55933 | 10 μM | ATM | 4 hours | 0.26994365 |
| LJI308 | 10 μM | RSK | 4 hours | 9.62544E-07 |
| CHIR99021 | 1 μM | GSK3 | 4 hours | 0.309440886 |
| KN62 | 10 μM | CaMK-II, P2RX7 | 4 hours | 0.021582087 |
| KU57788 | 1 μM | DNA-PK | 4 hours | 0.385979985 |
| Y27632 | 10 μM | ROCK | 4 hours | 0.375473038 |

**Supplementary Table T1.** Details of kinase inhibitors used.